# Analysis, Design, and Implementation of a Static Conductance-Based MPPT Method

Oswaldo Lopez-Santos, *Senior Member, IEEE*, Germain Garcia, Luis Martinez-Salamero, *Senior Member, IEEE*, Roberto Giral, *Senior Member, IEEE*, Enric Vidal-Idiarte, *Member, IEEE*, Maria Camila Merchan-Riveros, *Student Member, IEEE*, and Yamel Moreno-Guzmán

***Abstract*—This paper introduces a maximum power point tracking (MPPT) method based on a power (*P*) versus static conductance (*G*) curve of a photovoltaic (PV) array. The maximum power point (MPP) is tracked by comparing the PV array instantaneous power to a varying power reference generated by the MPPT algorithm. The comparison error is used to reduce or increase the conductance at which the PV array is forced to operate until the MPP is reached. Simultaneously, the error is used to change the power reference until the trajectory of this reference in the *P–G* curve enters a limit cycle around the MPP. The *P–G* curve is derived from a piecewise linear approximation of the current versus voltage (*I–V*) curve, which facilitates the analytical description of the tracking operation. The technique reported can also be implemented by means of simple analog or digital circuitry and requires two sensors to measure the instantaneous PV array current and voltage. It uses only four tuning parameters, which are selected depending on the maximum value of the derivative of the power with respect to the conductance. The theoretical predictions are verified with simulations and experimental results. The latter shows that the procedure performs well enough to be favorably compared with the most efficient MPPT methods.**

***Index Terms*—Extremum-seeking control, maximum power point tracking (MPPT), photovoltaic generators, power–conductance (*P–G*) curve.**

Manuscript received May 3, 2017; revised November 28, 2017 and February 16, 2018; accepted May 3, 2018. Date of publication May 14, 2018; date of current version December 7, 2018. This work was supported in part by the Spanish Agencia Estatal de Investigación under project DPI2016-80491-R (AEI/FEDER, UE) and in part by the Universidad de Ibagué under project #14-315-INT. Recommended for publication by Associate Editor J. A. Cobos. *(Corresponding author: Oswaldo Lopez-Santos.)*

O. Lopez-Santos is with the Programa de ingeniería Electrónica, Facultad de Ingeniería, Universidad de Ibagué, Ibagué 730001, Colombia (e-mail:

derivatives means that they are limited by the presence of noise and singularities in the numerical operations. A third group uses algorithms that work with an error signal between the maximum or a fictitious maximum and the actual operational point in order to impose a trajectory toward the real maximum of the function. These algorithms are called peak-holding, peak-searching, or peak-detection and are widely applied in many areas of engineering. This group includes fuzzy-logic [31]–[34], predictive [35], and random search methods [36]. Other methods such as ripple correlation control can be regarded as ESC methods [37] because they use a natural oscillatory component and the knowledge of its behavior around the optimum of the function to drive the system to the desired operational point [38], [39]. ESC includes many different methods [40]–[44], some of which use a sliding-mode (SM) strategy to ensure that the maximum is reached. These MPPT techniques are known in the literature as sliding-mode extremum seeking control (SM-ESC) methods [45]–[49] and, among other advantages, perform well and are easily integrated with the control of the dc–dc power converters. It is also worth mentioning that the estimation algorithm of the MPP reported in [50] does not need to track the point because it identifies in real time the complete current–voltage characteristics of the panel from the measurements of six voltage and current coordinates near the operating point.

The latest advances and contributions in the field of MPPT focus on the problem of partial shadowing, which involves multiple maximum points in the power versus voltage (*P–V*) characteristic, which transforms the problem into the tracking of the global MPP [51]–[54]. Nevertheless, all those solutions that improve existing ones or develop new ways to track a single MPP continue to be the object of interest in research into photovoltaic generation [55]–[61]. Current efforts focus on the rapidity, robustness, simplicity, and feasibility of these new solutions, only a few of which can be implemented with both analog and digital electronic circuitry.

Most of the MPPT methods mentioned use power versus voltage or power versus current curves to explain their corresponding algorithms. The output of the algorithms reduces or increases the value of the voltage or the current at which the PV generator is forced to operate. The decision is often illustrated by the resulting trajectory of the PV generator operating point along these curves. One example of this is the INC approach, which is based on the fact that the slope of the PV generator power curve (i.e., power versus voltage or power versus current) is zero at MPP, positive on the left and negative on the right. The MPP is tracked by comparing the instantaneous conductance of the PV generator to the INC so that the voltage at which the PV array is forced to operate in a power versus voltage curve decreases or increases depending on the result of the comparison. The behavior is similar in a power versus current curve when the value of the current at which the PV is forced to operate is changed. Two sensors are required to measure the instantaneous PV generator current and voltage, and a DSP or a microcontroller to implement the algorithm which explicitly uses derivatives and divisions.

The work reported here presents an MPPT method that explains tracking with a power (*P*) versus static conductance (*G*) curve of a solar array. The algorithm generates a varying power reference, which is compared with the PV array instantaneous power. The comparison error is processed to change the operating point of the array by modifying its static conductance until the MPP is reached. The error is used simultaneously to alter the power reference until the trajectory of the latter in the *P–G* curve attains a rhomboidal limit cycle around the MPP. The technique proposed can be categorized as ESC because it internally generates the oscillating signals required to bring the system to its MPP.

A piecewise linear approximation of the current versus voltage (*I–V*) curve of the PV array is used to derive the *P–G* curve, which eventually facilitates the analytical description of the tracking operation.

The technique proposed can also be implemented analogically or digitally. These implementations require the instantaneous measurement of the current and voltage of the PV array. Neither derivatives nor divisions are used.

The method is illustrated by matching the static conductance of a PV generator and the static input conductance of a quadratic boost converter that constitutes the first stage of a solar microinverter. The quadratic boost converter transfers the energy from the PV generator to a 400 dc regulated bus that eventually supplies a grid-connected full-bridge inverter.

The conductance is matched by imposing loss-free-resistor behavior on the quadratic boost converter by means of sliding-mode control [62]–[64]. The resulting static input conductance of the quadratic boost converter relates the input voltage and input current on the switching surface used in the sliding-mode control. The value of this conductance is the MPP conductance and is provided by the proposed MPPT. Fig. 1(a)–(c) illustrates the main ideas involved in the conductance matching. The regulation scheme is based on a two-loop control approach, in which the inner loop uses a sliding-mode strategy to impose proportionality between the input voltage and input current in the quadratic boost converter. The outer loop is based on the MPPT, which uses the measured voltage and current values of the PV array to generate the appropriate value of the static conductance required by the inner loop. The goal of the outer loop is to provide the optimal value of G (Gopt) that will result in the intersection of the *I–V* curve of the PV array and the curve of the dc characteristics of the converter input port [see Fig. 1(b)]. Since the converter is a two-port POPI (dc input power equal to dc output power) [65], the power absorbed at the converted input port will be transferred to the dc link at the output port [see Fig. 1(c)], where the resulting operating point in the dc bus is the intersection of the hyperbola corresponding to the absorbed power and the vertical straight line representing the constant voltage of the dc link.

The rest of the paper is organized as follows. Section II states the problem and introduces the MPPT algorithm, which is analyzed in detail in Section III. In particular, a stability analysis yields the main conditions the algorithm parameters must satisfy. These conditions involve the maximum of the slope of the *P–G* characteristic, which is evaluated in Section III. In Section IV, the sliding-mode LFR control applied to the dc–dc converter is briefly recalled and used in Section V to validate

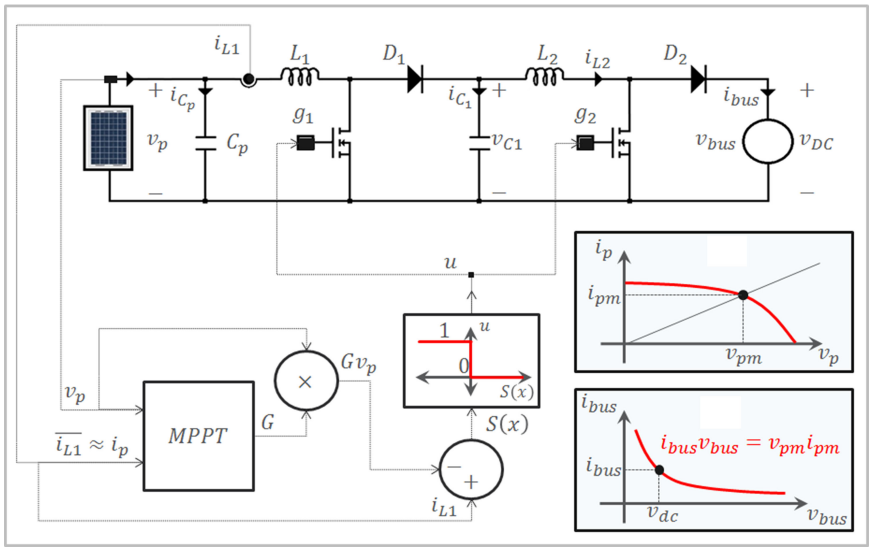


Fig. 1. (a) Block diagram illustrating the impedance matching of a PV array and a regulated dc bus using a quadratic boost converter as power interface. (b) Intersection of PV array and converter characteristics at MPP (Point M). (c) Operating point of the regulated dc bus.

the proposed MPPT algorithm by means of simulation and experiment. Subsequently, the proposed method is compared with other methods in Section VI. Finally, the conclusions are summarized in Section VII.

## II. Problem Statement

The current or the power delivered by a PV module can be modeled as a function of the output voltage as shown in Fig. 2. For a given PV module, it can be observed that different *I–V* and *P–V* curves (four in Fig. 2) can be obtained, each one of which corresponds to an irradiance level. In this context, $v_{\text{mpp}}$ denotes the voltage of the PV module at the MPP of the *P–V* characteristic, and the corresponding current is $i_{p\,\text{mpp}}$. These two characteristic curves are considered by most MPPT methods and can be used to derive geometrical approximations that facilitate the mathematical analysis [66]. The MPP for a given irradiance level $E_p$ also has a corresponding conductance value at the MPP $(G_{\text{mpp}})$ which can be derived from the relation between the current and voltage of the PV module at the MPP. Hence, the MPPT problem can also be solved if the input conductance of the power converter is forced to be equal to the conductance of the PV module at the MPP.

Considering the above remarks, the MPP can be tracked using the *P–G* characteristic of the PV module. As can be easily demonstrated, the *P–G* characteristic can be ideally defined for all positive values of conductance between zero and infinity.

The panel voltage range extends from zero (short-circuit) to open-circuit voltage. However, the practical range can be limited by the presence of the dc–dc switching converter matching the panel and the load. The limitation is apparent when the matching operation is modeled by a dc–dc transformer whose transformer ratio is the converter static gain, i.e., a function of the duty cycle. This situation appears when the MPPT is based on a power (*P*) versus voltage (V) PV curve, which is used to modify the duty cycle in order to eventually change the operating point of the panel. In the case considered here, the load is a 400 V dc regulated bus that would impose a limited excursion of the duty cycle, and therefore of the input voltage, if a dc–dc transformer-based approach was used.

In the proposed method, the limits of the panel voltage range are represented by a zero value of the conductance (open-circuit voltage) and an infinite value of the conductance (short-circuit) in the power (*P*) versus static conductance (*G*) curve. However, the dc–dc switching converter does not limit the excursion between the extreme points of the range. This is because the converter matching operation is modeled by a loss-free resistor (LFR), i.e., the converter input port can be emulated by a resistor whose conductance can take any value between zero and infinite. Besides, the LFR exhibits a nature of power source at the converter output port, the output power being the power absorbed by the emulated resistor at the input port. Therefore, the 400 V dc regulated bus absorbs the current supplied by the power source for any value of the voltage panel between zero and the open-circuit voltage.

The proposed MPPT uses conductance $G$ as the manipulated variable to force the input conductance of a dc–dc converter to be equal to the conductance of the PV module at the MPP$(G_{\text{mpp}})$. Because of the variable structure nature of the proposed MPPT, the instantaneous power of the PV module $P_p(t)$ is forced to remain in the neighborhood of the average value of an internal power reference$P_{p_{\text{ref}}}(t)$ which permanently tracks the MPP. Note that $P_p(t)$ is the real power delivered by the panel while $P_{p_{\text{ref}}}(t)$ is an auxiliary variable created by the control algorithm to track the MPP.

## III. Proposed MPPT Method

The proposed MPPT method has two fundamental objectives: 1) to eliminate the error $\varepsilon(t) = P_{p_{\text{ref}}}(t) - P_p(t)$ thus ensuring that the internal power reference $P_{p_{\text{ref}}}(t)$ is tracked, and 2) to guarantee that the reference $P_{p_{\text{ref}}}(t)$ increases automatically

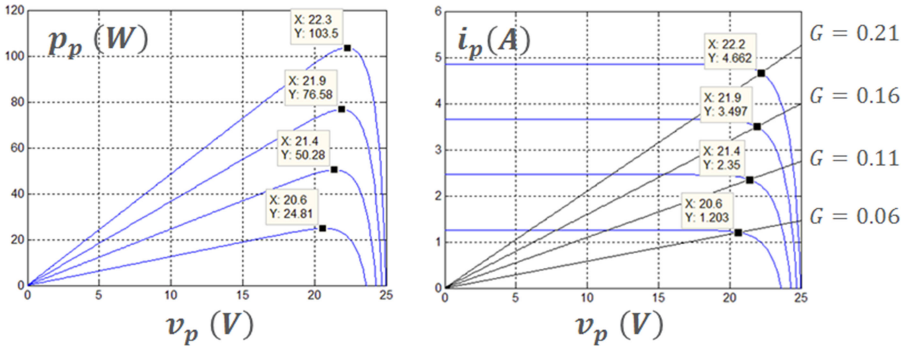


Fig. 2. *I–V* and *P–V* characteristics of a PV module.

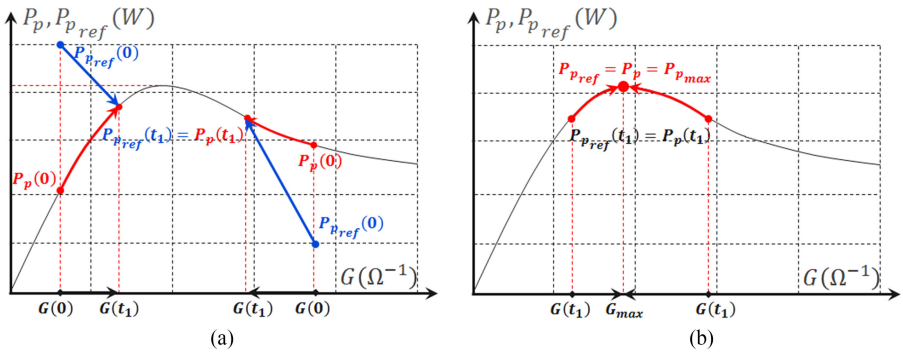


Fig. 3. Trajectories of the two objectives of the MPPT on the *P–G* plane.

until it reaches the maximal power $P_{\rm mp}$ where it is maintained. These objectives can be achieved by modifying the conductance $G(t)$ (see Fig. 3).

Fig. 3(a) considers two cases of initialization: i.e., to the left and to the right of the MPP. In both situations, the real power tracks the internal reference and both signals reach the maximum value [see Fig. 3(b)].

In addition, when there is an abrupt change in irradiance, a discontinuous change in $P_p(t)$ is observed and the reference $P_{p_{\rm ref}}(t)$ must be automatically redefined so that it converges on the new MPP. A block diagram representing the proposed MPPT is given in Fig. 4. The block diagram is structurally identical to the one reported in [67], the first paper to discuss self-optimization based on sliding-mode control. However, in our proposal the nonlinear functions of the error $u(\varepsilon)$ and $v(\varepsilon)$ are different, and the panel is characterized by the power versus conductance characteristics instead by the power versus converter duty cycle. As a result, no sliding-motions are induced in the proposal but the complete resulting dynamics can be explained analytically and therefore the criteria for MPPT parameter selection are clearly derived.

The algorithm uses the instantaneous value of the panel power $P_p(t)$, which is obtained from the current and voltage measurements in the PV panel. The MPPT also uses the error $\varepsilon$ relating $P_p(t)$ and the auxiliary variable $P_{p_{\rm ref}}(t)$.

The PV operating point, and hence $P_p(t)$, is changed by modifying the static conductance $G$ of the panel. This conductance is a triangular signal with positive slope when $G$ increases and with negative slope when $G$ decreases. Note that $G$ is a triangular signal because it is the integral of a square waveform whose levels are given by either $+P_p$ or $-P_p$, depending on the sign of $\varepsilon$.

$P_{p_{\rm ref}}(t)$ is also a triangular signal because it is the integral of a square waveform whose levels can be $+K_2P_p$ or $-(M-K_2)P_p$, with $M > K_2$, depending on the sign of $\varepsilon$. As shown in the next section and Appendix, the error $\varepsilon$ tends to zero in finite time, thus, resulting in an equilibrium point wherein the panel power corresponds to MPP, i.e., $P_p(t) = P_{\max}$, while $P_{p_{\rm ref}}(t)$ equals $P_p(t)$. However, when the nonlinear function $v(\varepsilon)$ is modified by the insertion of a hysteresis band, it is the average value of $P_{p_{\rm ref}}(t)$ which equals $P_p(t) = P_{\max}$ in the equilibrium point as demonstrated in Section III-B.

The equations associated with the block diagram above can be expressed as

$$\frac{dG}{dt} = f_1\left(P_p, u\right) \tag{1}$$

$$\frac{dP_{p_{\rm ref}}}{dt} = f_2\left(P_p, v\right) \tag{2}$$

$$f_1\left(P_p, u\right) = K_1 P_p u, \quad K_1 > 0 \tag{3}$$

$$f_2\left(P_p, v\right) = K_2 P_p + M P_p v, \quad K_2 > 0, \quad M > 0 \tag{4}$$

$$\varepsilon\left(t\right) = P_{p_{\rm ref}}(t) - P_p\left(t\right) \tag{5}$$

$$u = \text{sign}\left(\varepsilon\right) \tag{6}$$

$$v = -\frac{1}{2} - \frac{1}{2}\text{sign}\left(\varepsilon\right). \tag{7}$$

The functions $u$ and $v$ are represented in Fig. 5.

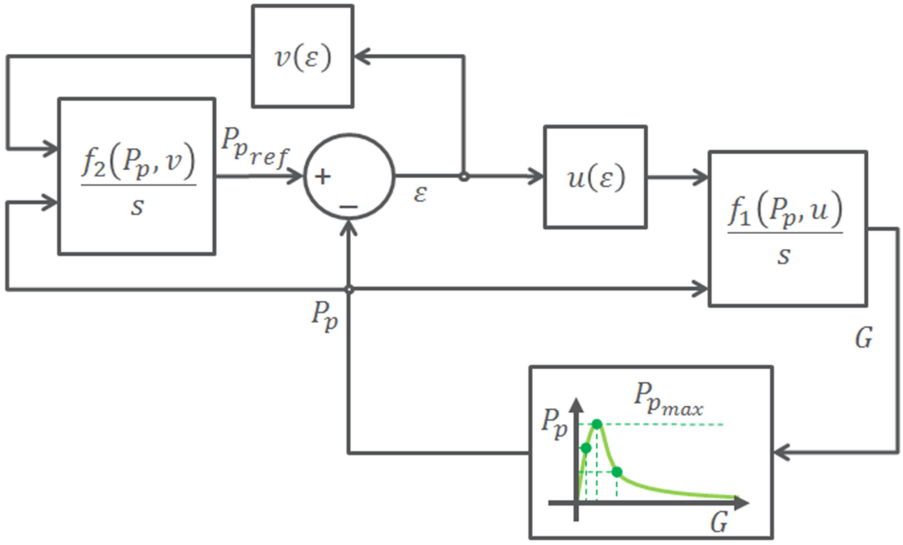


Fig. 4. Block diagram of the proposed self-optimized MPPT algorithm based on *P–G* characteristics.

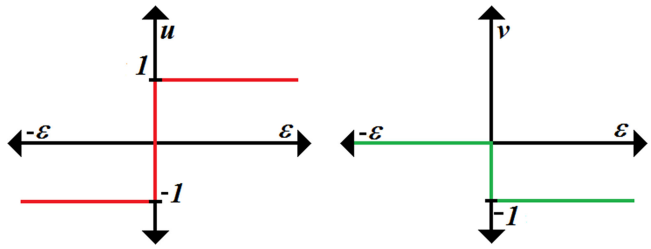


Fig. 5. Ideal switching functions of the proposed MPPT.

### A. *Regulation for* $\varepsilon = 0$.

First, the conditions for the stability of the regulation law $P_p = P_{p_{\text{ref}}}$ are analyzed. This requires that the conditions constants $M$, $K_1$, and $K_2$ must satisfy to guarantee a zero regulation error be determined. Consider the quadratic Lyapunov function

$$\mathrm{V}(\varepsilon) = \frac{1}{2}\varepsilon^2. \tag{8}$$

Stability is ensured if $\frac{dV}{dt} = \varepsilon\dot{\varepsilon} < 0$. Therefore

$$\varepsilon\dot{\varepsilon} = \varepsilon P_p \left[-\frac{1}{2}M - \frac{1}{2}M\ \text{sign}(\varepsilon) + K_2 - \frac{dP_p}{dG}K_1 \text{sign}(\varepsilon)\right] \tag{9}$$

but $\varepsilon = |\varepsilon|\text{sign}(\varepsilon)$ and $|\varepsilon| = \varepsilon \cdot \text{sign}(\varepsilon)$. Then

$$\begin{aligned}\varepsilon\dot{\varepsilon} &= P_p \left[-\frac{1}{2}M\varepsilon - \frac{1}{2}M|\varepsilon| + K_2\varepsilon - \frac{dP_p}{dG}K_1|\varepsilon|\right] \\ &= |\varepsilon| P_p \left[-\frac{1}{2}M\text{sign}(\varepsilon) - \frac{1}{2}M + K_2\text{sign}(\varepsilon) - \frac{dP_p}{dG}K_1\right].\end{aligned} \tag{10}$$

1) If $\varepsilon > 0$

$$\varepsilon\dot{\varepsilon} = |\varepsilon| P_p \left[-M + K_2 - \frac{dP}{dG}K_1\right]. \tag{11}$$

$$\text{If } M > K_2 + \left|\frac{dP_p}{dG}\right|_{\max} K_1 \text{ then } M > K_2 - \frac{dP_p}{dG}K_1 \text{ and } \varepsilon\dot{\varepsilon} < 0. \tag{12}$$

2) If $\varepsilon < 0$

$$\varepsilon\dot{\varepsilon} = |\varepsilon| P_p \left[-K_2 - \frac{dP_p}{dG}K_1\right]. \tag{13}$$

$$\text{If } K_2 > \left|\frac{dP_p}{dG}\right|_{\max} K_1 \text{ then } K_2 > -\frac{dP_p}{dG}K_1 \text{ and } \varepsilon\dot{\varepsilon} < 0. \tag{14}$$

In conclusion, the conditions for guaranteeing $\varepsilon\dot{\varepsilon} < 0$ are

$$M > K_2 + \left|\frac{dP_p}{dG}\right|_{\max} K_1 \text{ and } K_2 > \left|\frac{dP_p}{dG}\right|_{\max} K_1. \tag{15}$$

The above conditions show that the error tends to zero at least asymptotically. In practice, equilibrium needs to be reached in finite time. The appropriate stability notion in this situation is so-called finite time stability, which is reviewed in Appendix I. It is also demonstrated that $\varepsilon(t)$ attains $\varepsilon = 0$ in finite time [68].

It is worth mentioning that the previous conditions only depend on knowing $|\frac{dP_p}{dG}|_{\max}$, which can be obtained from the *P–G* curve, and, in particular, from the asymptotic approximation presented below in Section III-E. In the subsequent analysis, we consider that the parameters of the MPPT satisfy the above stability conditions. Hence, if $P_{\text{Pref}}(t)$ changes and the stability conditions are satisfied, $P_p(t)$ will track the reference $P_{\text{Pref}}(t)$. Now it is necessary to determine under what conditions the MPPT increases $P_{\text{Pref}}(t)$ until it reaches the MPP.

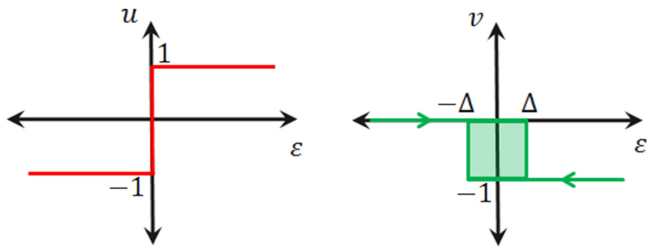


Fig. 6. Switching functions of the proposed MPPT.

### B. Convergence Toward the MPP

To analyze the evolution of $P_{\mathrm{P_{ref}}}(t)$, the nonlinear function $v(\varepsilon)$ is modified by inserting a hysteresis band while $u$ remains ideal (see Fig. 6).

At time $t_0$, $v=0$ and $u=1$. The error increases until it reaches the value $\Delta$ at time $t_1$ (i.e. $\varepsilon(\mathrm{t}_1)=\Delta$). At $t_1^+$, $v=-1$ and $u=1$ and the error decreases from $\Delta$ to $-\Delta$, which it reaches at time $t_3$ (i.e. $\varepsilon(t_3)=-\Delta$). But at time $t_2$ (between instants $t_1$ and $t_3$), the error crosses zero and at instant $t_2^+$, $u=-1$ and $v=-1$ [see Fig. 7(a)]. At time $t_3^+$, $v=0$ and $u=-1$. The error then increases until it reaches the value $\Delta$, but at time $t_4^+$, the error crosses zero and changes the value of $u$ $(u=1)$, with $v$ remaining equal to zero. Then the system returns to the initial configuration $v=0$, $u=1$, etc. To sum up, the trajectory associated to $\varepsilon$ depends on the repeated sequence presented at the bottom of Fig. 7(b) with the associated time intervals. The resulting waveforms of $P_{p_{\mathrm{ref}}}(t)$, $G(t)$, $v(t)$, and $u(t)$ induced by the repeated sequences in the *P–G* characteristic curve are shown in Fig. 7(b). If $P_{p_{\mathrm{ref}}}(t_4)>P_{p_{\mathrm{ref}}}(t_0)$, after completing a sequence, then $P_{p_{\mathrm{ref}}}(t)$ will increase toward the MPP.

The dynamical equations describing the motion of $P_{p_{\mathrm{ref}}}(t)$ and $G(t)$ for each time interval can be easily calculated using (1)–(4). They are summarized in Table I.

On the other hand, the time derivative of the error can be expressed as

$$\frac{d\varepsilon}{dt}=\frac{dP_{p_{\mathrm{ref}}}}{dt}-\frac{dP_p}{dt}=\left[\frac{dP_{p_{\mathrm{ref}}}}{dG}-\frac{dP_p}{dG}\right]\frac{dG}{dt}. \tag{16}$$

Taking into account the expressions in Table I, (16) can be particularized for the different states of the basic tracking sequence (see Table II).

From the stability conditions in (15), it can be derived that

$$\left.\frac{d\varepsilon}{dt}\right|_{(1,0)}>0,\quad \left.\frac{d\varepsilon}{dt}\right|_{(1,-1)}<0,\quad \left.\frac{d\varepsilon}{dt}\right|_{(-1,-1)}\left\langle 0,\quad \left.\frac{d\varepsilon}{dt}\right|_{(-1,0)}\right\rangle 0. \tag{17}$$

This result is in accordance with the waveform of Fig. 7. If $\Delta$ is assumed to be small, $P_p$ and $\frac{dP_p}{dG}$ will not significantly vary within the range of lengths $\Delta$. Consequently, they can be regarded as practically constant in this range. Taking into account the equations describing the motion of $\varepsilon$, the following expressions are deduced

$$\begin{aligned}
t_1-t_0&\cong\frac{\Delta}{\left[K_2-K_1\frac{dP_p}{dG}\right]P_p}\\
t_2-t_1&\cong\frac{\Delta}{\left[M-K_2+K_1\frac{dP_p}{dG}\right]P_p}\\
t_3-t_2&\cong\frac{\Delta}{\left[M-K_2-K_1\frac{dP_p}{dG}\right]P_p}\\
t_4-t_3&\cong\frac{\Delta}{\left[K_2+K_1\frac{dP_p}{dG}\right]P_p}.
\end{aligned} \tag{18}$$

Using the expressions of the time derivatives of the error in Table I, the variation of $P_{P_{\mathrm{ref}}}$ can be easily evaluated in the interval $[t_0,t_4]$ as follows:

$$\begin{aligned}
P_{\mathrm{P_{ref}}}(t_4)\cong&P_{\mathrm{P_{ref}}}(t_0)+K_2P_p(t_1-t_0)+(K_2-M)P_p(t_2-t_1)\\
&+(K_2-M)P_p(t_3-t_2)+K_2P_p(t_4-t_3)\\
=&P_{\mathrm{P_{ref}}}(t_0)+K_2P_p(t_4-t_0)-MP_p(t_3-t_1).
\end{aligned} \tag{19}$$

After some simple algebraic calculations, we obtain

$$\begin{aligned}
&K_2P_p(t_4-t_0)-\mathrm{M}P_p(t_3-t_1)=\Delta\\
&\times\left[\frac{2K_2^2}{K_2^2-K_1^2\left(\frac{dP_p}{dG}\right)^2}-\frac{2(M-K_2)^2}{(M-K_2)^2-K_1^2\left(\frac{dP_p}{dG}\right)^2}\right]\\
&=\Delta\left[f(K_2)-f(M-K_2)\right]
\end{aligned} \tag{20}$$

where $f(x)$ is defined by

$$f(x)=\frac{2x^2}{x^2-a^2}\quad\text{with } a=K_1\frac{dP_p}{dG}. \tag{21}$$

The derivative of $f(x)$ is given by

$$\begin{aligned}
\frac{df(x)}{dx}&=\frac{4x\left(x^2-a^2\right)-2x^2(2x)}{\left(x^2-a^2\right)^2}\\
&=\frac{-4a^2x}{\left(x^2-a^2\right)^2}\langle 0\ \text{ if } x\rangle 0 \text{ and } x\neq a.
\end{aligned} \tag{22}$$

If $f(K_2)-f(M-K_2)>0$, this will imply $P_{p_{\mathrm{ref}}}(t_4)>P_{p_{\mathrm{ref}}}(t_0)$. Since the derivative of $f$ is negative, $K_2$ and $M-K_2\neq K_1\frac{dP_p}{dG}$ from stability conditions, it can be concluded that $f(K_2)-f(M-K_2)>0$ if and only if $M-K_2>K_2$, which can also be written as $M>2K_2$. Adding this inequality to the above stability conditions yields all the constraints that parameters $M$, $K_1$, and $K_2$ must satisfy. They can be summarized as follows:

$$M>2K_2 \text{ and } K_2>\left.\left|\frac{dP_p}{dG}\right|\right|_{\max}K_1. \tag{23}$$

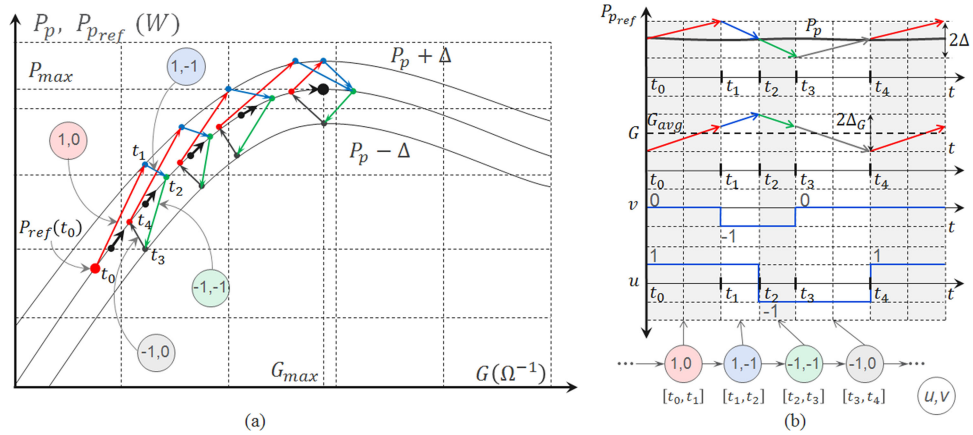


Fig. 7. (a) MPP tracking sequences on the *P–G* curve. (b) Resulting waveforms related with tracking sequences.

TABLE I
DERIVATIVES OF $P_{p\,\mathrm{REF}}$ AND $G$ IN THE BASIC MPP TRACKING SEQUENCE

| u,v | Differential equations describing the dynamic behavior of $P_{p_{ref}}$ and G | |
|---|---|---|
| 1,0 | $\left.\frac{dP_{p_{ref}}}{dt}\right\|_{(1,0)} = K_2 P_p$<br>$\left.\frac{dG}{dt}\right\|_{(1,0)} = K_1 P_p$ | $\left.\frac{dP_{p_{ref}}}{dG}\right\|_{(1,0)} = \frac{K_2}{K_1}$ |
| 1,-1 | $\left.\frac{dP_{p_{ref}}}{dt}\right\|_{(1,-1)} = [K_2 - M]P_p$<br>$\left.\frac{dG}{dt}\right\|_{(1,-1)} = K_1 P_p$ | $\left.\frac{dP_{p_{ref}}}{dG}\right\|_{(1,-1)} = \frac{K_2 - M}{K_1}$ |
| -1,-1 | $\left.\frac{dP_{p_{ref}}}{dt}\right\|_{(-1,-1)} = [K_2 - M]P_p$<br>$\left.\frac{dG}{dt}\right\|_{(-1,-1)} = -K_1 P_p$ | $\left.\frac{dP_{p_{ref}}}{dG}\right\|_{(-1,-1)} = \frac{M - K_2}{K_1}$ |
| -1,0 | $\left.\frac{dP_{p_{ref}}}{dt}\right\|_{(-1,0)} = K_2 P_p$<br>$\left.\frac{dG}{dt}\right\|_{(-1,0)} = -K_1 P_p$ | $\left.\frac{dP_{p_{ref}}}{dG}\right\|_{(-1,0)} = -\frac{K_2}{K_1}$ |

TABLE II
MODELING OF THE MPPT POWER ERROR

| u,v | Differential equations describing the dynamic behavior of $\varepsilon$ |
|---|---|
| 1,0 | $\left.\frac{d\varepsilon}{dt}\right\|_{(1,0)} = \left[\frac{K_2}{K_1} - \frac{dP_p}{dG}\right] K_1 P_p = \left[K_2 - K_1 \frac{dP_p}{dG}\right] P_p$ |
| 1,-1 | $\left.\frac{d\varepsilon}{dt}\right\|_{(1,-1)} = \left[\frac{K_2 - M}{K_1} - \frac{dP_p}{dG}\right] K_1 P_p = \left[K_2 - M - K_1 \frac{dP_p}{dG}\right] P_p$ |
| -1,-1 | $\left.\frac{d\varepsilon}{dt}\right\|_{(-1,-1)} = \left[\frac{M - K_2}{K_1} - \frac{dP_p}{dG}\right] (-K_1 P_p) = \left[K_2 - M + K_1 \frac{dP_p}{dG}\right] P_p$ |
| -1,0 | $\left.\frac{d\varepsilon}{dt}\right\|_{(-1,0)} = \left[-\frac{K_2}{K_1} - \frac{dP_p}{dG}\right] (-K_1 P_p) = \left[K_2 + K_1 \frac{dP_p}{dG}\right] P_p$ |

From the above analysis, $P_{\mathrm{P_{ref}}}(t)$ increases until it reaches the vicinity of $P_{\mathrm{mp}}$, where it imposes the condition $P_p \cong P_{\mathrm{mp}}$. Then

$$\frac{d\,P_{\mathrm{P_{ref}}}}{dt} \cong \frac{d\,P_p}{dt} \cong \frac{dG}{dt} \cong 0 \text{ and therefore } f_1(P_p, u) = 0, f_2(P_p, v) = 0. \tag{24}$$

Hence, from (3) and (4), the average values $\bar{u}$ and $\bar{v}$ of $u$ and $v$ will be given by

$$\bar{v} = -\frac{K_2}{M} > -1 \text{ and } \bar{u} = 0. \tag{25}$$

### C. Influence of Parameters $\Delta$, $M, K_1$, and $K_2$

This section discusses the performance of the proposed algorithm and evaluates the influence of the parameters $\Delta$, $M, K_1$ and $K_2$. The period $T_p$ of the oscillation around the power $P_p$ is equal to $t_4 - t_0$. Then it can be expressed as

$$T_p = \frac{2K_2\Delta/P_p}{K_2^2 - K_1^2\left(\frac{dP_p}{dG}\right)^2} + \frac{2(M - K_2)\Delta/P_p}{(M - K_2)^2 - K_1^2\left(\frac{dP_p}{dG}\right)^2}. \tag{26}$$

When the algorithm reaches $P_{\mathrm{mp}}$, then $\frac{dP_p}{dG} \cong \frac{dP_{p\,\mathrm{ref}}}{dG} \cong 0$. Hence

$$T_p = T_{\mathrm{mp}} = \frac{2\Delta M}{K_2(M - K_2)P_{\mathrm{mp}}}. \tag{27}$$

The associated frequency is given by

$$f_{\mathrm{mp}} = \frac{K_2(M - K_2)P_{\mathrm{mp}}}{2\Delta M} \tag{28}$$

where $\Delta$ and $K_2$ are constant.

Considering the constraints $2K_2 < M < \infty$, then $f_{\mathrm{mp}} \in \left]\frac{K_2 P_{\mathrm{mp}}}{4\Delta}, \frac{K_2 P_{\mathrm{mp}}}{2\Delta}\right[$. Hence, the frequency $f_{\mathrm{mp}}$ can be controlled by appropriately selecting the parameters $\Delta$, $M$, and $K_2$. Now, the amplitude of the fluctuations of the power reference around the maximum point $P_{\mathrm{mp}}$ is evaluated. Its determination is illustrated in Fig. 8.

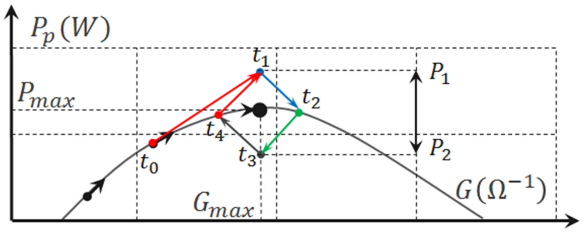


Fig. 8. Determination of the amplitude of power reference and conductance at the MPP.

From Table I, the amplitude of the oscillation in the power reference shown in Fig. 8 will be given by

$$\Delta P_{\mathrm{P_{ref}}} = P_{\mathrm{P_{ref}}}(t_1) - P_{\mathrm{P_{ref}}}(t_3) = -(K_2 - M)\,P_p(t_2 - t_1) - (K_2 - M)\,P_p(t_3 - t_2) = (M - K_2)\,P_p(t_3 - t_1) = \frac{2(M-K_2)^2\Delta}{(M-K_2)^2 - {K_1}^2\left(\frac{dP_p}{dG}\right)^2}. \quad (29)$$

At the MPP $\frac{dP_p}{dG} \cong 0$ and, therefore, $\Delta P = P_1 - P_2 = 2\Delta$, as expected. The parameter $\Delta$ is the only parameter used to express the amplitude of power fluctuations. Hence, the conductance is constrained to lie in a band of width $\Delta G = G(t_2) - G(t_4)$ given by

$$\Delta G = K_1 \frac{\Delta M}{\left[M - K_2 - K_1\frac{dP_p}{dG}\right]\left[K_2 + K_1\frac{dP_p}{dG}\right]}. \quad (30)$$

At the MPP, $\frac{dP_p}{dG} \cong 0$, which implies

$$\Delta G = \frac{K_1 \Delta M}{(M - K_2)\,K_2} \quad (31)$$

considering the constraints $2K_2 < M < \infty$, then $\Delta G \in \left]\frac{K_1\Delta}{K_2}, \frac{2\,K_1\Delta}{K_2}\right[$.

It can be concluded that the value of $\Delta$ controls the amplitude of the power fluctuations around $P_{\mathrm{mp}}$ and that three parameters, namely, $M, K_1$ , and $K_2$, can be used to regulate the frequency and the conductance fluctuations around the maximum. From (23) and (31), it can be observed that the smaller $K_1$ is, the more insensitive the algorithm is to $|\frac{dP_p}{dG}|_{\max}$, and the weaker the effect on the variation of $\Delta G(t)$. Nonetheless, this effect must be sufficient to guarantee that MPPT behaves well.

Moreover, the value of $\Delta$ has a significant influence over both static and dynamic performances of the algorithm. A low value of $\Delta$ implies high values of tracking efficiency but also high duration of the transient state to reach a new MPP after a sudden change of irradiance. Besides, it is worth mentioning that a value of $M$ broadly satisfying inequality (23), e.g., $M$ between four and ten times higher than $K_2$, improves the rapidity and tracking efficiency of the algorithm.

### D. Behavior Under Variations in Irradiance

When irradiance is constant, the characteristics of the power of a PV module are represented by a single curve, which is described here as a function of the conductance (*P–G*). Now, we describe the behavior for variations in irradiance.

*Increase in irradiance:* Before the change, $P_{P_{\mathrm{ref}}}(t)$ is at maximum admissible power (for example $P_{\mathrm{mp1}}$ in Fig. 9). Due to this abrupt change at $t_1$, $P_p(t)$ suffers a discontinuity and the panel characteristic curve suddenly changes. The power of this new curve is higher for all values of $G$. In this case, we have $\varepsilon(t_1^+) = P_{p_{\mathrm{ref}}}(t_1^+) - P_p(t_1^+) < 0$. For $t_1^+ > t_1 + \delta$, where $\delta$ is positive, we have

$$\frac{dP_{\mathrm{P_{ref}}}(t)}{dt} = K_2 P_p(t) > 0 \text{ and } \frac{dG(t)}{dt} = -K_1 P_p(t) < 0 \quad (32)$$

$P_{P_{\mathrm{ref}}}(t)$ is increasing and $G(t)$ is decreasing, so $P_p(t)$ is decreasing until it is equal to $P_{P_{\mathrm{ref}}}(t)$ at $t_2$. From the analysis in the sections above, $P_{P_{\mathrm{ref}}}(t)$ and $P_p(t)$ will move toward the new maximum, which they reach at $t_3$ (see Fig. 9).

*Decreasing irradiance:* With the same notations as before, we have $\varepsilon(t_1^+) = P_{p_{\mathrm{ref}}}(t_1^+) - P_p(t_1^+) > 0$. For $t_1^+ > t_1 + \delta$, where $\delta$ is positive, we have

$$\frac{dP_{\mathrm{P_{ref}}}(t)}{dt} = (K_2 - M)P_p(t) \left\langle 0 \text{ and } \frac{dG(t)}{dt} = K_1 P_p(t) \right\rangle 0. \quad (33)$$

$P_{P_{\mathrm{ref}}}(t)$ is decreasing and $G(t)$ is decreasing, so $P_p(t)$ is decreasing until it is equal to $P_{P_{\mathrm{ref}}}(t)$ at $t_2$. From the analysis in the sections above, $P_{P_{\mathrm{ref}}}(t)$ and $P_p(t)$ will move toward the new maximum, which they reach at $t_3$ (see Fig. 10).

The analysis of the algorithm is now complete. Even if there are sudden changes in irradiance, the proposed algorithm makes it possible to extract the maximum power of the PV module, provided that $|\frac{dP_p}{dG}|_{\max}$ is correctly evaluated. The analysis in the section below gives the value of $|\frac{dP_p}{dG}|_{\max}$ and makes it possible to select the constants $\Delta, M, K_1$, and $K_2$.

### E. Approximation of $|\frac{dP_p}{dG}|_{\max}$

The *I–V* and *P–V* characteristics of the solar panel are crucial to solve the MPPT problem.

Because of the complexity of the mathematical models that define these characteristics, some methods work with approximations to reduce the complexity of the controller synthesis [69]. In this paragraph, the objective is to asymptotically approximate the *I–V* and the *P–V* characteristics of a PV module in order to determine the *P–G* characteristic curve.

As shown in Fig. 11(a), the *I–V* characteristic curve of a PV module can be approximated by two asymptotes. They are defined using the short-circuit current $(I_{\mathrm{sc}})$, the open-circuit voltage $(V_{\mathrm{oc}})$ and the voltage corresponding to the maximum power $(V_{\mathrm{mp}})$.

Using this approximation, the *I–V* characteristic is defined by

$$i_p(v_p) = \begin{cases} I_{\mathrm{sc}} & 0 < v_p < V_{\mathrm{mp}} \\ -G_0\,(v_p - V_{\mathrm{oc}}) & V_{\mathrm{mp}} < v_p < V_{\mathrm{oc}} \end{cases} \quad (34)$$

where $G_0 = I_{\mathrm{sc}}/(V_{\mathrm{oc}} - V_{\mathrm{mp}})$. The *P–V* characteristic can be deduced by multiplying the previous approximation by $v_p$. The

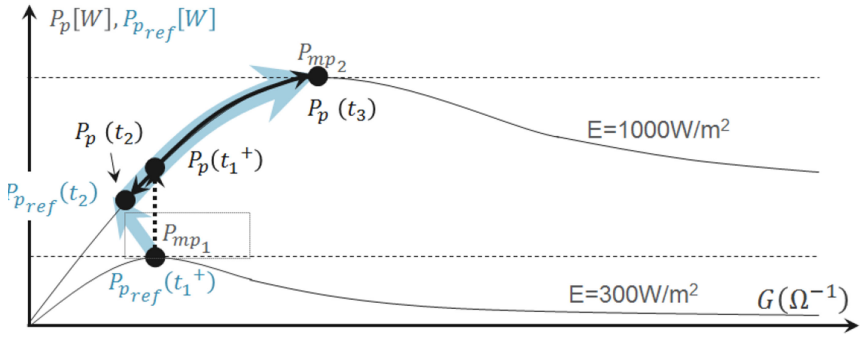


Fig. 9. Trajectories in the plane *P–G* after a sudden positive change in irradiance.

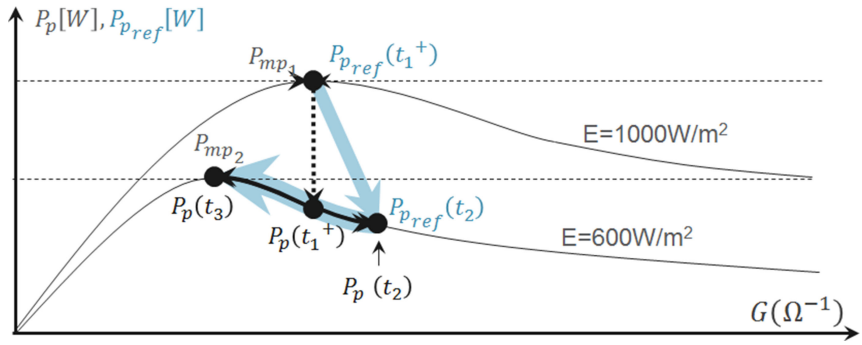


Fig. 10. Trajectories in the plane *P–G* after a sudden negative change in irradiance.

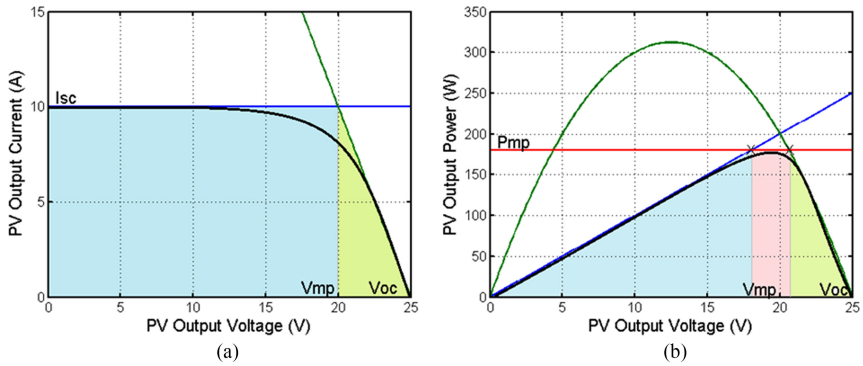


Fig. 11. Asymptotic approach of the characteristic curves of the PV module. (a) *I–V*. (b) *P–V*.

two asymptotes are transformed into the curves depicted in Fig. 11(b). In order to improve the approximation, a third asymptote corresponding to the maximum attainable power ($P_{\rm mp}$) is introduced. An analytical expression for the derived approximation follows and is given by

$$p_p\left(v_p\right) = \begin{cases} I_{\rm sc} v_p & 0 < v_p < V_1 \\ P_{\rm mp} & V_1 < v_p < V_2 \\ -G_0\left(v_p^2 - V_{\rm oc} v_p\right) & V_2 < v_p < V_{\rm oc} \end{cases} \tag{35}$$

where $V_1 = P_{\rm mp}/I_{\rm sc}$ and

$$V_2 = 0.5\ {\rm V_{oc}} + \sqrt{0.25\ {\rm V_{oc}^2} - P_{\rm mp}(V_{\rm oc} - V_{\rm mp})/I_{\rm sc}}.$$

In order to obtain the *P–G* characteristic, the variable *G*, which is defined as $G = i_p/v_p$ is introduced in the previous approximation. Since $v_p^2 = p_p/G$, (38) becomes

$$p_p\left(G\right) = \begin{cases} G_0^2 V_{\rm oc}^2 \frac{G}{(G+G_0)^2} & 0 < G < G_1 \\ P_{\rm mp} & G_1 < G < G_2 \\ \dfrac{I_{\rm sc}^2}{G} & G_2 < G < \infty \end{cases} \tag{36}$$

where $G_2 = I_{\rm sc}^2/P_{\rm mp}$ and

$$G_1 = (G_0^2 V_{\rm oc}^2[1 - \sqrt{1 - 4P_{\rm mp}/(V_{\rm oc}^2 G_0)}] - 2G_0 P_{\rm mp})/2P_{\rm mp}.$$

The resulting characteristic is depicted in Fig. 12.

By obtaining the derivatives of (36) and finding their maximum values in their corresponding ranges, it is deduced that the

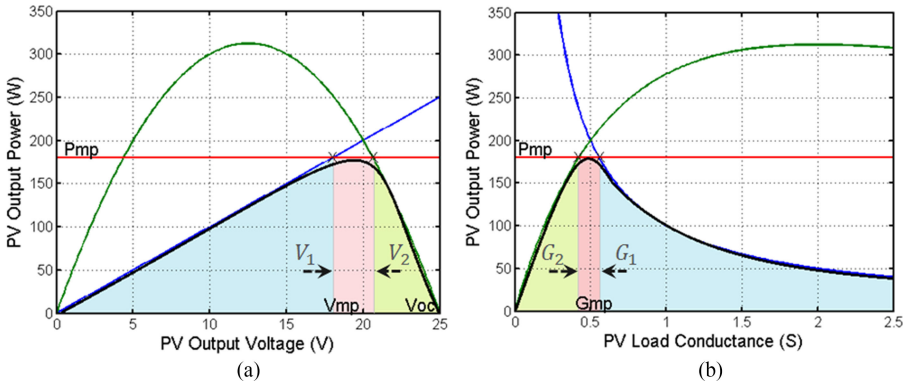


Fig. 12. Asymptotic approach of the characteristic curves of the PV module. (a) *P–V*. (b) *P–G*.

maximum derivative satisfies the following inequality:

$$\frac{dP_p}{dG}_{\max} < \max\left\{\left(\frac{P_{\rm mp}}{I_{\rm sc}}\right)^2, V_{\rm oc}^2\right\} \tag{37}$$

where the maximum computed value using (37) is always above the maximum derivative of the real curve.

## IV. Microinverter, DC–DC Converter, and Input Conductance Control

A two-stage microinverter has been selected as the application for the proposed MPPT method. The power stage of the microinverter consists of a quadratic boost converter on the input side and a full-bridge inverter on the output side [70]. As depicted in Fig. 1(c), the output of the dc–dc converter is a power source which supplies the dc link of the microinverter, whose voltage is regulated by the dc–ac stage. This behavior in the quadratic boost converter can be accomplished by using a Sliding Mode controller to force the converter to operate as an SM-LFR. This control uses a given conductance value to induce sliding motions in the input current of the converter. The proposed MPPT tracks the value of the required conductance to permanently extract the maximum power of the PV module. Then, the control of the dc–dc converter uses the conductance computed by the MPPT on the sliding surface given by the following expression:

$$S(x) = i_{\rm in}(t) - v_p(t)\,G(t). \tag{38}$$

The output voltage of the dc–dc converter does not have a regulation loop acting from the dc–dc converter variables so its value depends on the load. The conductance reference given by the MPPT is quickly imposed on the dc–dc converter by the SM-LFR control and is independent of the load behavior. So, the dc–ac stage can be considered by the dc–dc converter to be a constant voltage load. However, the dc-link voltage contains a double grid frequency component which perturbs the PV module voltage through the reverse audio-susceptibility of the dc–dc converter. Since the paper focuses on the MPPT method, only a general description of the dc–dc converter operation is given. Fig. 13 illustrates the block diagram of the resulting system for the impedance matching of the PV panel and the regulated dc bus using the quadratic boost converter as LFR for power interfacing. The main parts of the block diagram are the result of introducing the MPPT scheme of Fig. 4 into the block diagram of Fig. 1(a).

Note that two low-pass filters have been added to remove the ac components of the current and voltage measurements. For the current, the ac component is the ripple at the switching frequency whereas for the voltage the ac component is introduced by the equivalent series resistor of the coupling capacitor at the input of the dc–dc converter due to the back propagation of the double grid frequency ripple. The cut-off frequencies of these filters must be selected to prevent these high- and low-frequency variations from affecting the MPPT operation and causing a malfunction.

It should also be pointed out that a hysteresis comparator is preferred to an ideal one in Fig. 13 to constrain the switching frequency of the converter to a finite variable value. This depends on the input and output voltages of the converter and a hysteresis band with limits of $\pm\delta$ [71].

## V. Simulated and Experimental Results

In order to verify the theoretical prediction of the MPPT behavior, a set of simulations was implemented in PSIM using the parameters listed in Table III.

As can be seen in Table III, a PV module with values of 5 V in the open-circuit voltage and 5 A in the short-circuit current was selected to adapt the *I–V* characteristic to the range values used in a digital implementation. The dc–dc stage was simulated as a controlled current source whose value is defined by the product of the conductance given by the MPPT and the measured voltage of the PV module. A capacitor of 10 $\mu$F was connected in parallel with the module. Based on the shaded parameters in Table III and (37), the maximum derivative is approximated as $|\frac{dP_p}{dG}|_{\max} = 17$. The parameters of the MPPT were chosen to be $K_1 = 0.2$, $K_2 = 10$, $M = 40$ in order to satisfy the conditions defined by (15) considering $\Delta = 0.1P_{p_{\max}} = 2$ for a selected $f_{\rm mp} \approx 40$ Hz.

### A. Steady State of the PV Module and MPPT Variables

Fig. 14 shows the steady-state waveforms when an average power of 19.36 W is supplied by the PV module. The operation at the MPP is confirmed because of the double frequency of the power function. The efficiency of the MPPT operating in steady-state or tracking factor, as calculated in [72]–[74], is given by

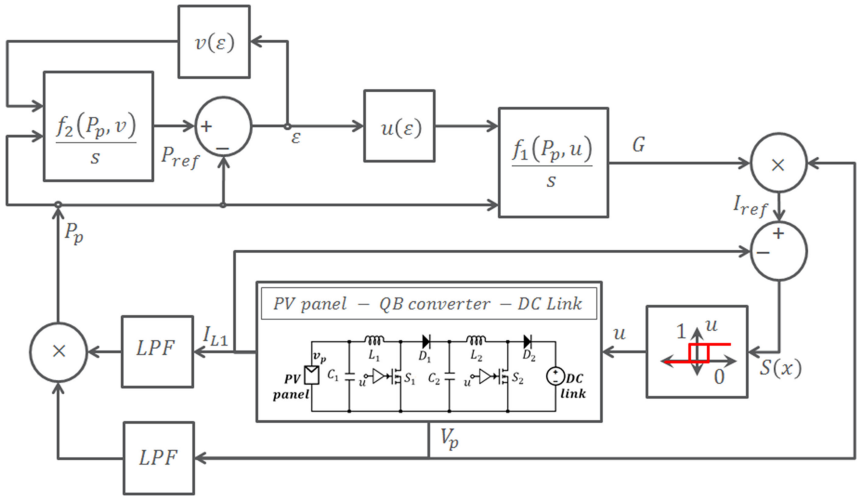


Fig. 13. Block diagram integrating the PV module, dc–dc converter, SM-LFR controller, and MPPT.

TABLE III
PARAMETERS OF THE SIMULATED PV MODULE AT STANDARD TEST CONDITIONS (STC) TEMPERATURE = 25 °C AND IRRADIANCE E = 1000 W/M$^2$

| Parameter | Symbol | Value |
|---|---|---|
| Open-circuit voltage | $V_{oc}$ | 5 V |
| Short-circuit current | $I_{sc}$ | 5 A |
| Maximum power | $P_{mp}$ | 20.5 W |
| Voltage at $P_{mp}$ | $V_{mp}$ | 4.5 V |
| Current at $P_{mp}$ | $I_{mp}$ | 4.5 A |
| Slope at $V_{oc}$ | $dv/di(V_{oc})$ | -0.1 V/A |
| Series resistance | $R_s$ | 0.01 Ω |
| Shunt resistance | $R_{sh}$ | 1000 Ω |
| Saturation current | $I_{so}$ | 4.28x10$^{-14}$ A |
| Band energy | $E_g$ | 1.12 eV |
| Ideality factor | A | 1.2 |
| Temperature coefficient | $C_T$ | 0.00325 A/K |
| Number of cells | $N_s$ | 6 |

the following expression:

$$\eta_{\text{MPPT}}(t) = \frac{\int_0^t P_{p_{\text{actual}}}(\tau)\, d\tau}{\int_0^t P_{p_{\max}}(\tau)\, d\tau} \tag{39}$$

where $P_{\text{actual}}$ and $P_{p_{\max}}$ are the respective measured values of the actual power and the maximum power of a PV module during a time interval of duration $t$.

All the efficiency values presented in this paper refer only to MPPT performance and consequently do not include the efficiency of the converter. The efficiency of the MPPT is computed as 99.8%. The oscillatory components of the PV module variables have amplitudes of 100 mA (3.4%), 170 mV (4%) and 0.062 W (0.5%).

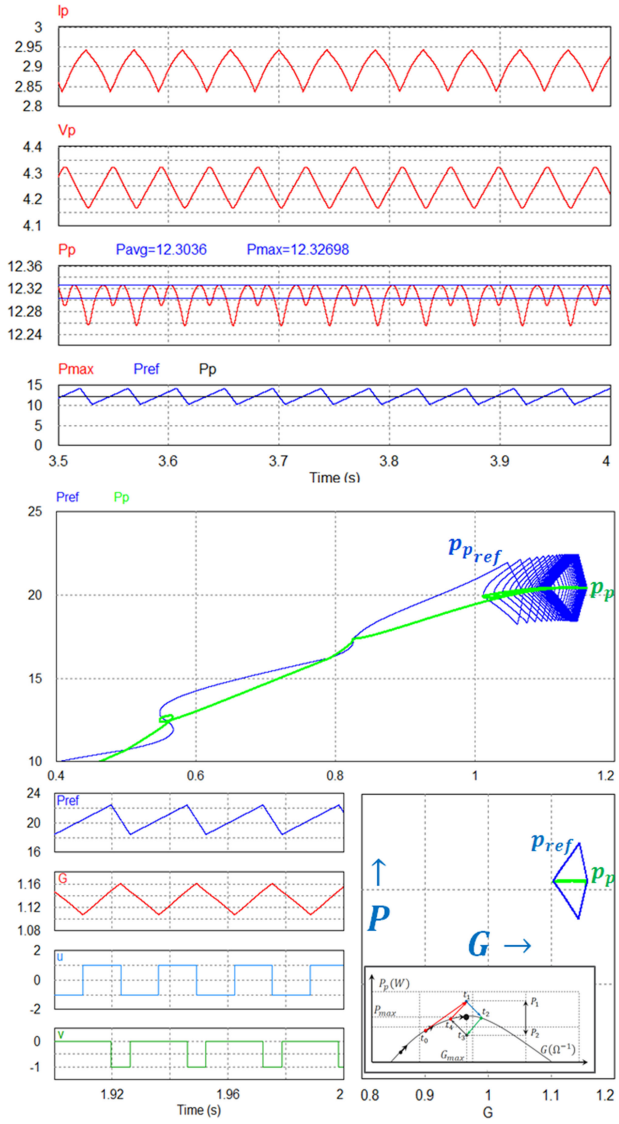


Fig. 14. Detail of the simulated oscillatory components of current, voltage, and powers.

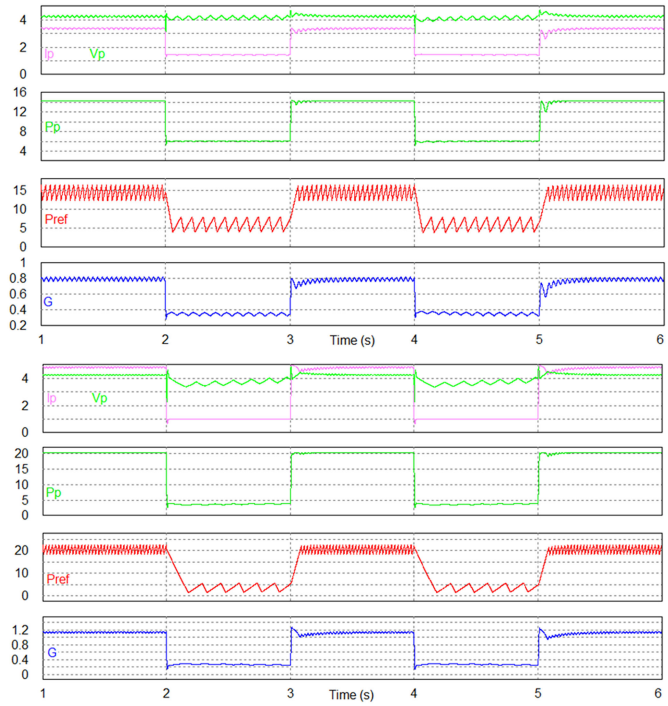


Fig. 15. Simulated results of the dynamic behavior of the algorithm dealing with sudden changes in irradiance between 300 and 700 W/m$^2$ and vice versa (top) and between 200 and 1000 W/m$^2$ and vice versa (bottom).

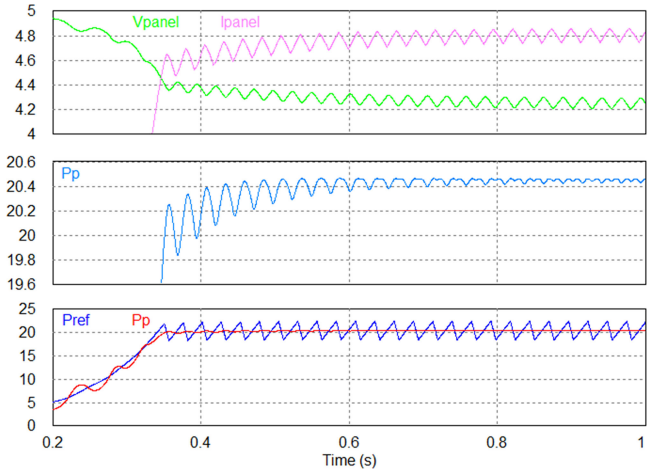


Fig. 16. Response of voltage, current, and power during system start-up.

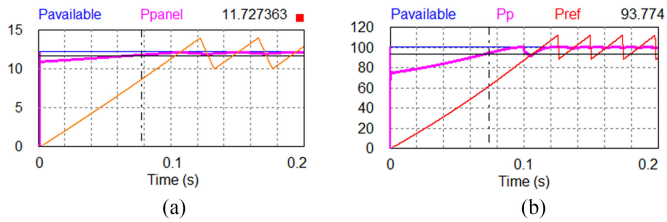


Fig. 17. Power response during system start-up when no low-pass filters are used. (a) PV module with maximum power of 12 W. (b) PV module with maximum power of 100 W.

Fig. 14 shows the trajectory of the power in the *P–G* plane toward the MPP. The power reference enters a limit cycle of rhomboidal type around the MPP when this point is reached by the output power. The steady state of the MPPT variables shows the relation between the time response and the *P–G* plane representation. The amplitude of the variations in the conductance is 0.05 S and the amplitude of the variations in the power reference is 4 W.

### *B. Dynamic Response to Changes in the P–V Characteristic*

Two simulations are used to assess the dynamic response of the MPPT. The first one is the four first waveforms in Fig. 15, which illustrate the effect of variations in irradiance in the solar module between 300 and 700 W/m$^2$ and vice versa. Each new state lasts for 1 s. The second simulation corresponds to the last four waveforms in the same figure and illustrates the effect of changes between 200 and 1000 W/m$^2$ and vice versa using the same time intervals.

As can be noted in both simulations, $P_p(t)$ quickly reaches the MPP and shows a smooth transient response when step disturbances are applied to the power. It is also worth noting that in both cases the system behaves similarly and, in general, performs well because maximum power is reached almost instantaneously after a power disturbance penetrates the system.

### *C. Start-Up of the MPPT*

In Fig. 16(a), simulation of the start-up of the MPPT variables illustrates the transient behavior from the starting point (zero current) to an equilibrium point corresponding to the maximum power. It can be observed that the steady state is reached in around 300 ms. Note that the power quickly reaches values in the neighborhood of the MPP, thus ensuring appropriate behavior.

It is important to note that during start-up, both the power reference and the measured power are very close, induced by the control law. Although they do not exhibit the same hysteretic behavior for the MPP, both signals oscillate around the MPP. It can be observed in the current and voltage waveforms that the fundamental component of the ripples has the same frequency as the power reference. As a consequence, the ripple in the power of the PV module has a component at the same frequency as the power reference and a component at double frequency, which can be differentiated in terms of the operating point coordinates. When the system operates at the MPP, the amplitude of the double frequency component is comparable with the fundamental component (see Fig. 16).

The settling time obtained in the start-up illustrated in Fig. 16 is affected by the low-pass filters used to measure the current and voltage required to compute the actual power. It is worth mentioning that these filters are not a part of the MPPT method and they are only used for the microinverter application. As can be observed in Fig. 17, when the low-pass filters are removed in two different cases, the power of the PV module approaches the amount of power available almost four times faster than in Fig. 16. There is no change in the power reference until the MPP has been attained. The time required to reach 90% of the power available is estimated to be less than 80 ms.

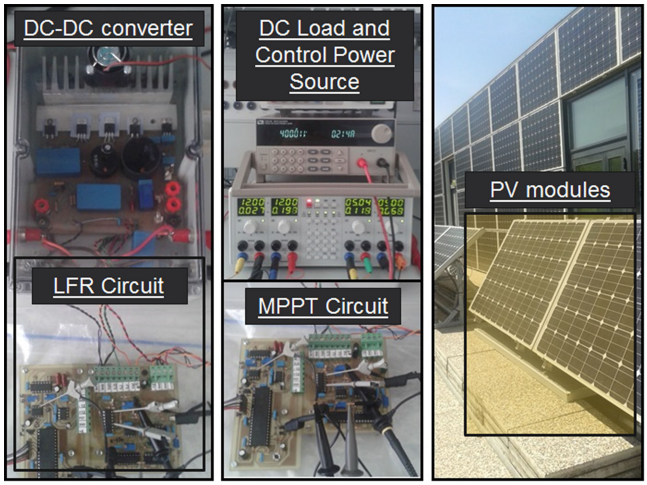


Fig. 18. Converter and MPPT prototype, experimental setup, and panel used in the experiments.

### D. Prototype and Experimental Setup

The MPPT and the SM-LFR control of the dc–dc converter was implemented using a dsPIC30F4011 microcontroller and some analog electronic circuits. The parameters of the quadratic boost converter are: input inductor $(L_1)$ of 120 $\mu$H, intermediate inductor $(L_2)$ of 4.7 mH, input capacitor of 9 $\mu$F, and intermediate and output capacitors ($C_1$ and $C_2$) of 9 $\mu$F [71]. The hysteresis is $\pm$0.5 A. It provides switching frequencies between 130 and 180 kHz for input voltages between 20 and 30 V. A constant sampling frequency of 50 kHz was used in the microcontroller. The serial digital-to-analog (DAC) converter MCP4812 was used to obtain the continuous signals $G$ and $P_{p_{\text{ref}}}$. Two digital pins of the micro-controller were used to reproduce the signals of the nonlinear functions $u$ and $v$ for the experiments. The setup for measurements, photovoltaic modules, the converter prototype, and the MPPT circuit are shown in Fig. 18. The experimental setup was constructed at the LAAS-CNRS's ADREAM building in Toulouse, France, a facility that researches renewable energies. The setup consisted of an E4360A solar panel emulator, an MSO3014 oscilloscope, TCP202 and TCPA300 current probes, an XA3033 power supply, an HP34401A multimeter, an IT8512B electronic load, an MP-160 *I–V* Curve Tracer, and two BP 585 solar panels whose characteristic parameters are listed in Table IV.

### E. Experimental Results

Fig. 19(a) shows the steady-state waveforms when an average power of 91.2 W is extracted from the PV emulator and injected into a voltage load of 400 V through a quadratic boost converter. The PV emulator was configured with an $I_{\text{sc}}$ of 4 A and a $V_{\text{oc}}$ of 25 V. The maximum derivative for this module was approximated using the asymptotic model to give $|\frac{dP_p}{dG}|_{\max} = 531$. Then, the parameters of the MPPT were chosen as $K_1 = 0.015$, $K_2 = 10$, $M = 90$, and $\Delta \approx 16$ W for a selected $f_{\text{mp}} = 25$ Hz. The double frequency of the power waveform in comparison with the frequency of the voltage and current waveforms confirms that the system works at the MPP (considering a single maximum operational condition). The oscilloscope capture shows the measured power $P_p$, which is compared with the power reference. Using (39) for a maximum power of 92.02 W and an average power of 91.2 W, an MPPT efficiency of 99.1% is obtained. The oscillating components of the PV module variables have amplitudes of 200 mA (5%), 1.6 V (6.6%), and 2.6 W (2.8%), respectively.

TABLE IV
PARAMETERS OF THE PV MODULE BP585 AT STANDARD TEST CONDITIONS (STC) TEMPERATURE = 25 °C AND IRRADIANCE = 1000 W/M$^2$

| Parameter | Symbol | Value |
|---|---|---|
| Open-circuit voltage | $V_{oc}$ | 22.1 V |
| Short-circuit current | $I_{sc}$ | 5 A |
| Maximum power | $P_{mp}$ | 85 W |
| Guaranteed minimum $P_{mp}$ | $P_{mp_{min}}$ | 80.8 W |
| Voltage at $P_{mp}$ | $V_{mp}$ | 18.0 V |
| Current at $P_{mp}$ | $I_{mp}$ | 4.72A |

The internal signals of the MPPT are also depicted for the MPP by comparing the time-based representation with the *P–G* representation. The four trajectories corresponding to the four structures of the system and the rhombus in steady state are clearly differentiated in Fig. 19(b). The waveforms on the left of Fig. 19(b) show the variation in the conductance and the power reference, and illustrate how the signals $u$ and $v$ induce the motion of the system.

Two tests were performed to assess the dynamic response of the MPPT. In the first test, the *I–V* characteristic of the panel emulator changed from a first curve with a maximum power of about 95 W to another curve with a maximum power of 65 W and vice versa. Each corresponding *I–V* characteristic curve is maintained for 500 ms. The waveforms obtained are shown in Fig. 19(c). In the second test, the *I–V* characteristic of the panel emulator changed from a first curve with a maximum power of about 110 W to another curve with a maximum power of 20 W and vice versa. The resulting waveforms are depicted in Fig. 19(d). In both tests, the MPPT showed a very rapid response. Furthermore, the panel power $P_p(t)$ reached the vicinity of the maximum value before the power reference, thus improving the general performance and the power harvesting.

### F. MPPT Performance Operating With the Whole Microinverter System

The general functionality of the MPPT was also experimentally evaluated using an overall microinverter system connected to the grid and fed by a solar panel. Fig. 20 shows an oscilloscope capture with the system's most representative waveforms. The maximum measured power was 82.24 W while the average power was 81.82 W. The MPPT efficiency computed for this experiment using (39) was 99.49%. The *P–V* characteristic curve of the panel shown in Fig. 20 was captured with the

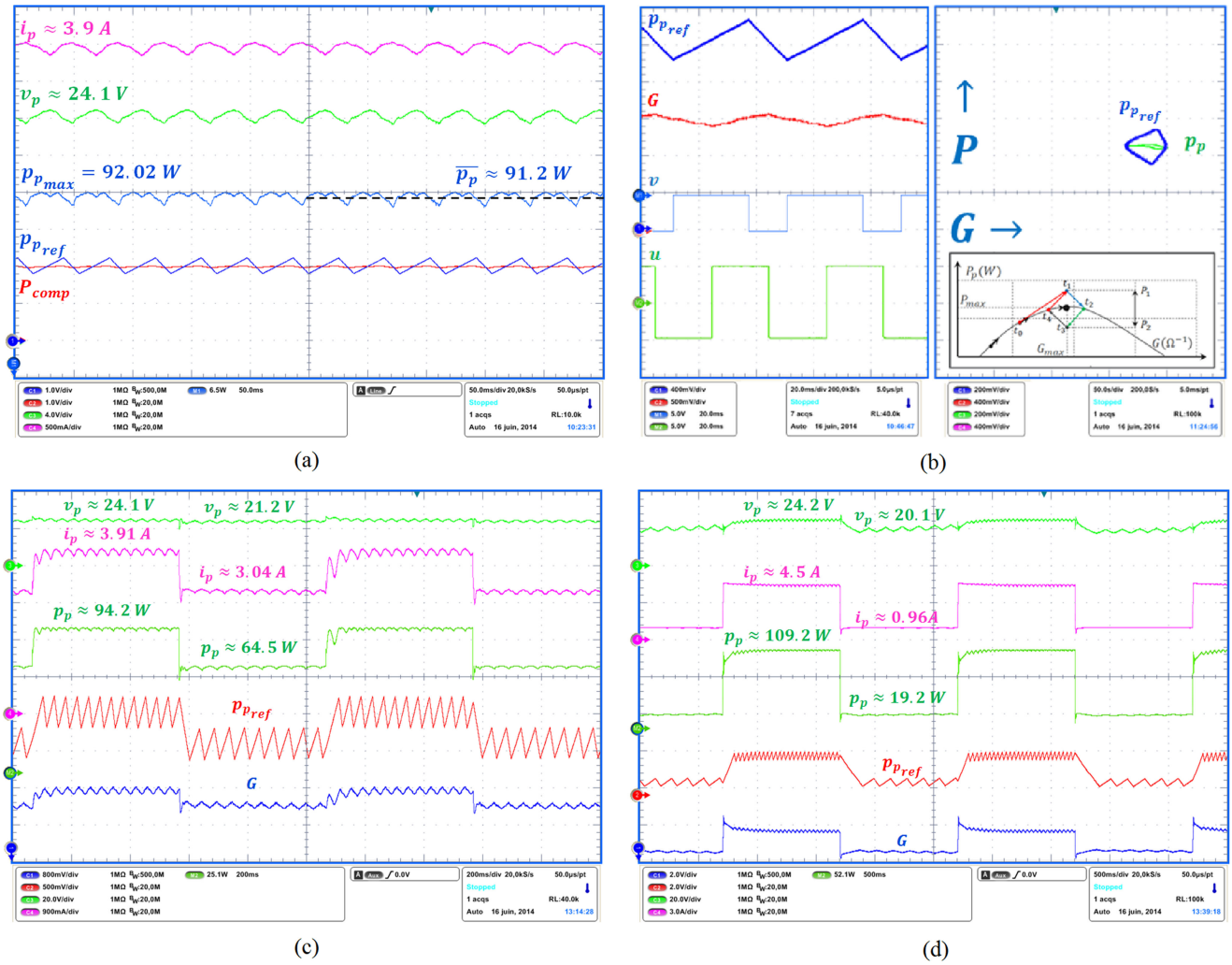


Fig. 19. Experimental results. (a) Steady state of the MPPT variables. (b) Steady state of the MPPT signals and representation in the *P*–*G* plane. (c) Transient response to 30 W power disturbances. (d) Transient response to 80 W power disturbances.

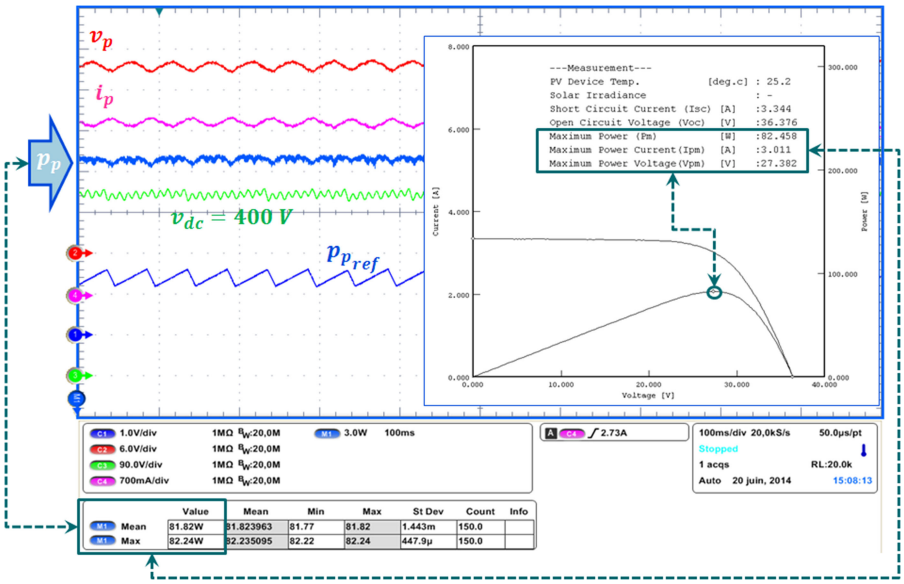


Fig. 20. General validation of the performance of the proposed MPPT.

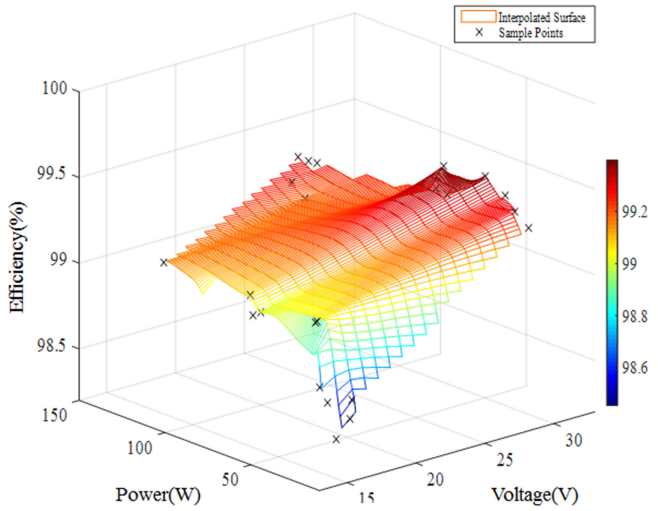


Fig. 21. Tracking efficiency versus voltage and power.

curve tracer EKO MP-160 and is presented here only for illustrative purposes. The oscilloscope capture shows the power waveform exhibiting the expected double frequency phenomenon at the MPP. The power reference and the voltage of the dc bus (400 V) were also measured.

### G. MPPT Efficiency for a Wide Range of Power and Input Voltage

Additional experiments were performed for different levels of voltage and power by measuring the efficiency in three cases, i.e., single solar panel, parallel connection, and series connection of two identical panels. The efficiency results are illustrated in Figs. 21 and 22 in three-dimensional and two-dimensional plots, respectively.

It can be observed in Fig. 21 that the efficiency is higher than 99% for a wide range of voltage and power values. This is also verified in Fig. 22(a) and (b), where the efficiency is plotted as a function of voltage and power, respectively. The efficiency increases in a monotonous way in the latter figures from a minimum of 98.2% to a maximum of 99.2%, which correspond respectively to the minimum and maximum values of both voltage and power in the test.

## VI. Discussion

In order to make this method comparable to other published methods (i.e., to ensure the same conditions and the optimal set of parameters in each case), a PSIM simulation was then performed. The aim of the simulation is to compare two previously reported ESC methods with the method proposed here (PMPPT) using the converter's input conductance as the manipulated variable in all cases. The first method (FESC) was presented in [44] and adapted to a sliding-mode control inner loop of a boost converter in [63]. In the application considered in [63], FESC also used the conductance of the converter as the manipulated variable but the MPPT algorithm was based on a $P$–$V$ curve and a differentiator had to be used. The second method (SM-ESC) is a variation of the method reported in [67]. This variation consists of using the input conductance of the converter instead of the duty cycle as the algorithm output.

In order to compare both steady-state and dynamic performances, a sequence of changes were applied during an interval of operation of 1 s. All algorithms started from zero initial conditions at $t = 0$ operating with 15% of a nominal irradiance of 1000 W/m$^2$. After reaching steady state, irradiance disturbances were applied at 0.2, 0.4, 0.6, and 0.8 s which increased and decreased the irradiance in the following sequence 15% $\rightarrow$ 70% $\rightarrow$ 45% $\rightarrow$ 100% $\rightarrow$ 55% (see Fig. 23). As can be observed, the proposed method not only gives the best response to sudden changes in irradiance in all cases, but it also yields the highest MPPT efficiency throughout the interval.

To refine the conclusion about the tracking efficiency, a zoom was made for specific values of irradiance for three intervals in steady state. As is depicted in Fig. 24, the proposed method shows that performance was best for low and high irradiance levels, and that it was only slightly less efficient than the SM-ESC method for medium levels (99.82% versus. 99.83%).

To situate the PMPPT in a broader context, we now use the values of the tracking factor in well-known MPPT methods reported in [73] for comparative purposes; namely, Gaussian-Arctangent Function based with variable perturbation frequency (GAF-VPF) (97.8%), variable step-size INC (VSSINC) (97.32%), fuzzy (96.50%) and load-current adaptive step size, and perturbation frequency (LCASF) (96.6%). It is commonly accepted that efficiencies above 99% are exceptional; hence, the tracking efficiency of the proposed MPPT is comparable with that of high performance methods. To reinforce this, we processed the measurements for an interval of almost 5 h. Computing (39) using an interval of 17 100 s gave an efficiency of 99.1% (see top of Fig. 25).

The efficiency is minimum for an MPP of 7 W (98.5%), and maximum for an MPP of 61 W (99.6%). This test confirms that the algorithm performs well for a wide range of operational conditions, especially at higher values of irradiance when the amount of power produced is greater. The data were acquired and analyzed with a computational application developed in LabVIEW, two 10-bit channels of a USB-6008 acquisition card, a sensor CAS-15 measuring the current of the PV module, and a simple voltage divider measuring the voltage of the PV module.

The comparative study presented in [73] shows that the best dynamic tracking factors reported are lower than 98% (i.e., below the value of 99.6% exhibited by the proposed algorithm). It should be pointed out that the evaluation interval used to calculate the dynamic performance of the proposed MPPT is long and irradiances are below 500 W/m$^2$ for more than half of the time, which is not in favor of a high tracking efficiency.

The possible ways that the proposed MPPT method can be implemented and its simplicity are also points that can be compared with other existing methods. As is summarized in [6], not all well-known MPPT methods are implementable in both analog and digital form. Likewise, they are not all equally complex to implement; they are highly dependent on the mathematical functions used. In a clear-cut contrast, the proposed method requires only a few multiplications, sums, integrals, comparisons, and gains, and can be implemented in either analog or

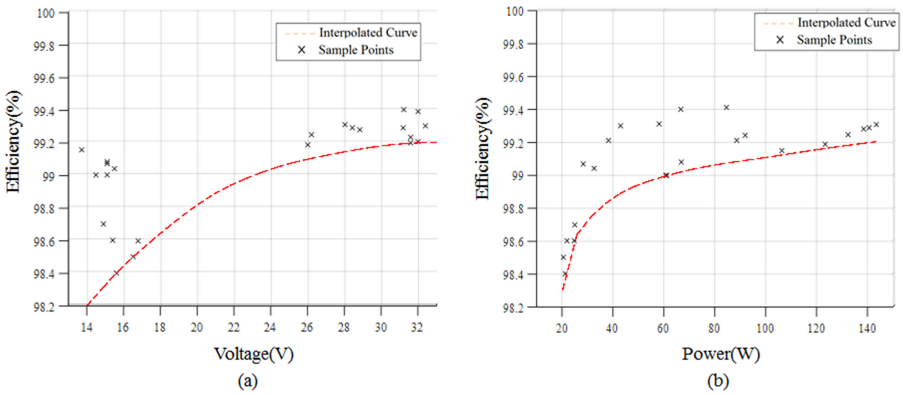


Fig. 22. (a) Tracking efficiency versus voltage. (b) Tracking efficiency versus power.

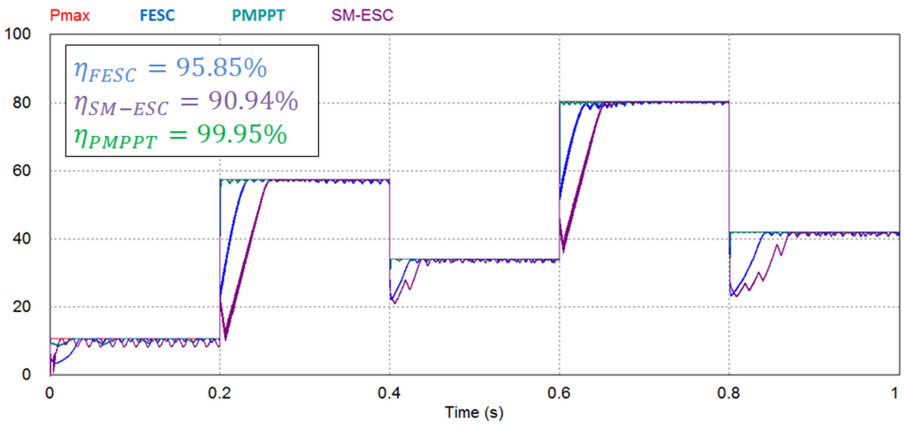


Fig. 23. Simulated results comparing static and dynamic performances of three ESC methods.

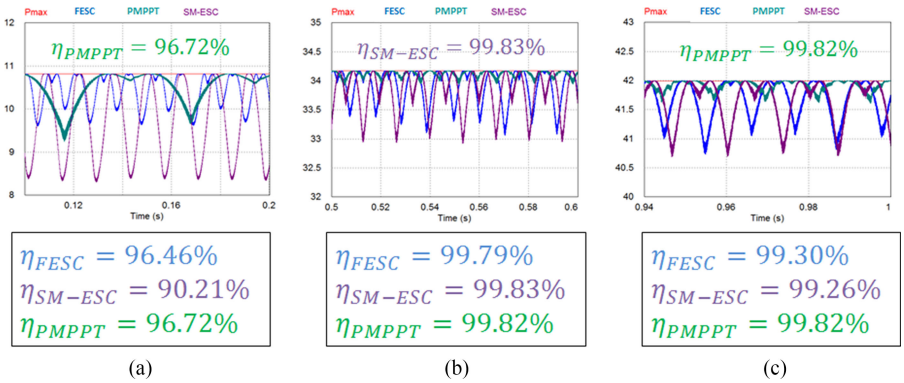


Fig. 24. PSIM simulations showing steady-state performance of the three MPPT methods for three different irradiance levels IR. (a) IR $= 150\,\mathrm{W/m^2}$. (b) IR $= 450\,\mathrm{W/m^2}$. (c) IR $= 550\,\mathrm{W/m^2}$.

digital circuits. In [55], which reports a fast and robust MPPT method, analog implementation is simpler because it requires only seven ICs, and some resistors and capacitors. In our proposal, nine ICs are required to implement both the MPPT method and the inner current control loop of the LFR; namely, three multipliers, three quad operational amplifiers, two quad comparators, and one dual flip-flop. Other methods require derivatives, divisions or even trigonometric functions, which makes the analog version unrealizable and the digital one much more complex.

This paper has shown how to obtain the rules and guidelines to select an appropriate set of parameters. These parameters are mainly obtained by estimating the maximum derivative of the power with respect to the conductance of a given PV module (based on nominal characteristics). Besides, for a specific PV module used in a MIC, for example, the estimated set of param-

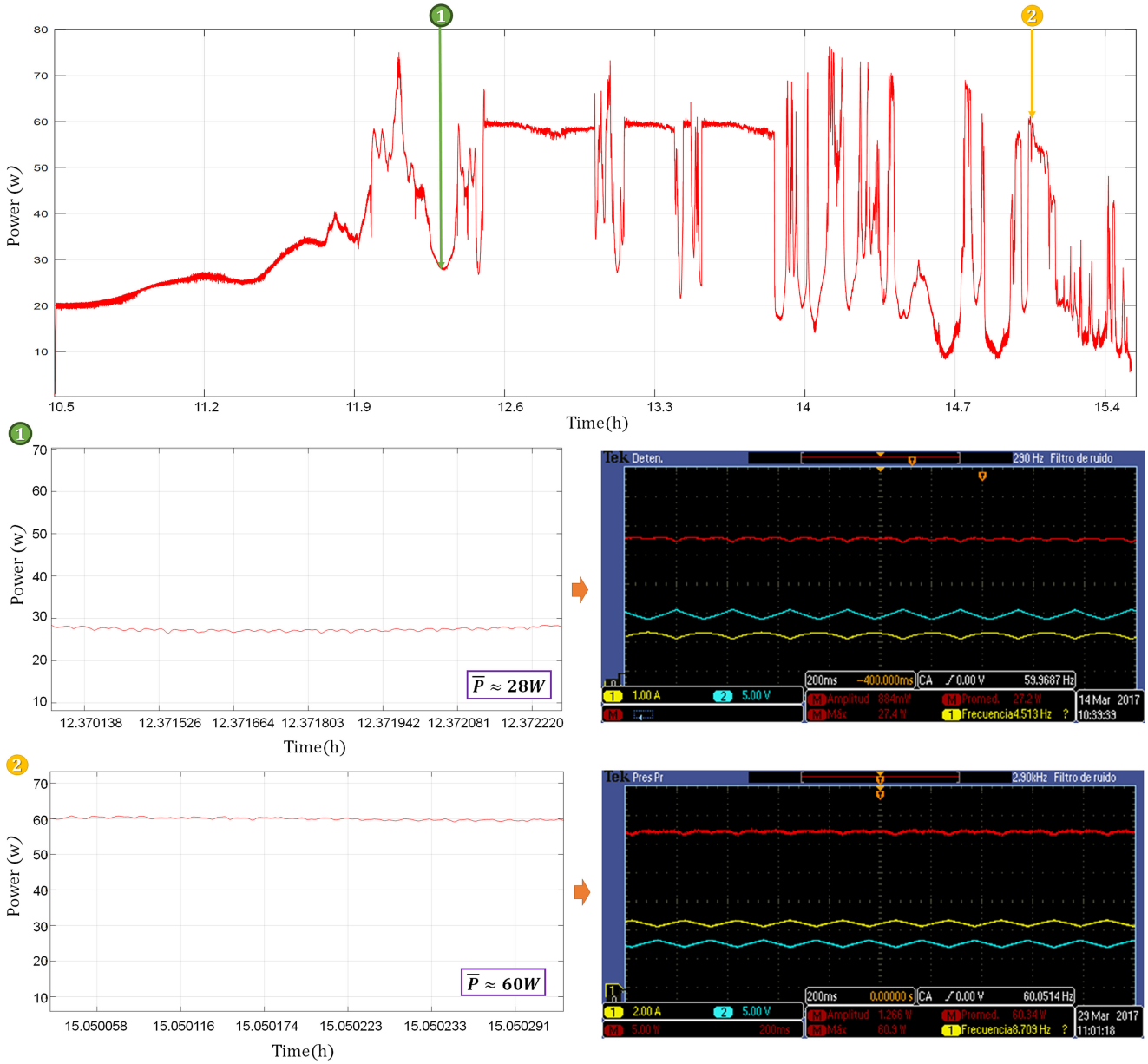


Fig. 25. Experimental results evaluating MPPT dynamic tracking factor for a long-time interval.

eters of the MPPT can be tuned so that efficiency and rapidity can be further optimized.

## VII. Conclusion

This paper has discussed an ESC-based MPPT, which has been studied analytically and described exhaustively. The stability of the control law and the trajectory toward the maximum point have been modeled, studied, and validated.

The novelty of the method lies in the fact that a power versus static conductance curve of the PV array is used to accurately track the MPP. The MPP is tracked by comparing the instantaneous power of the PV array to a varying power reference generated by the algorithm. The comparison error is used to change the power reference until it reaches the MPP in the *P–G* curve, and to decrease or increase the conductance at which the PV array is forced to operate. Besides, the instantaneous power determines the amplitude of the nonlinear functions $u(\varepsilon)$ and $v(\varepsilon)$ used in the algorithm, which explains the rapidity with which the tracking mechanism reacts to changes in irradiance.

The method requires only four tuning parameters ($K_1$, $K_2$, $M$, and $\Delta$), which are selected taking into account the maximum derivative of the power with respect to the conductance. It is also proposed that the derivative for a specific PV module can be evaluated using an asymptotic modeling of the PV module characteristics. As a consequence, the MPPT can be easily tuned to ensure that it operates correctly between 10% and 100% of the nominal power. The method can be implemented using both analog and digital electronics mainly because of the simplicity of the mathematical functions required.

The high performance of the MPPT was verified with simulation and experimental results. The latter show efficiency values above 98% with a maximum value of 99.6% for a wide range of voltage and power. The MPPT supports sudden changes in the power available and has proved to be robust and reliable. The method has been shown to be comparable with the most efficient MPPT methods reported in the literature.

## APPENDIX

From (1) to (5), we can deduce that

$$\frac{d\varepsilon}{dt} = \left[\frac{dP_{p\,\mathrm{ref}}}{dG} - \frac{dP_p}{dG}\right]\frac{dG}{dt} = f(\varepsilon)$$

and applying Theorem 4.2 in recalled here for completeness:

*Theorem:* Suppose there exists a continuous function $V(\varepsilon)$ such that the following conditions hold.

1) $V(\varepsilon)$ is positive definite.
2) There exist a number $C > 0$, $\alpha \in (0, 1)$, and an open neighborhood of the origin such that $\dot{V}(\varepsilon) + C(V(\varepsilon))^{\alpha} \leq 0$, $\varepsilon \neq 0$.

Then the origin is a finite-time-stable equilibrium. Moreover, the settling-time function satisfies

$$T_{\varepsilon} \leq \frac{1}{C(1-\alpha)}(V(\varepsilon))^{1-\alpha}.$$

From (11), (13), and $\boldsymbol{V}(\varepsilon) = \frac{1}{2}\varepsilon^2$ we have

$$\dot{\boldsymbol{V}}(\varepsilon) = \varepsilon\dot{\varepsilon} = |\varepsilon| P_p \left[-M + K_2 - \frac{dP}{dG}K_1\right]$$

or

$$\dot{\boldsymbol{V}}(\varepsilon) = \varepsilon\dot{\varepsilon} = \ |\varepsilon| P_p \left[-K_2 - \frac{dP_p}{dG}K_1\right].$$

Depending on the sign of $\varepsilon$. Let us define

$$C_1 = \left[M - K_2 + K_1\left|\frac{dP_p}{dG}\right|_{\max}\right] P_p\left(0^+\right) > 0$$

$$C_2 = \left[K_2 - K_1\left|\frac{dP_p}{dG}\right|_{\max}\right] P_p\left(0^+\right) > 0.$$

Where positivity follows from conditions in (15). Let $C_3 = \min\{C_1,\ C_2\}$. From (11) and (13), we can deduce that (remarking that $|\varepsilon| = \sqrt{2}[\boldsymbol{V}(\varepsilon)]^{\frac{1}{2}}$)

$$\dot{\boldsymbol{V}}(\varepsilon) + \sqrt{2}C_3[\boldsymbol{V}(\varepsilon)]^{\frac{1}{2}} = \dot{\boldsymbol{V}}(\varepsilon) + C[\boldsymbol{V}(\varepsilon)]^{\frac{1}{2}} \leq 0, \quad \text{for all } \varepsilon \neq 0.$$

From the previous theorem, the error $\varepsilon(t)$ is finite-time stable, meaning that $\varepsilon(t)$ attains $\varepsilon = 0$ in a finite time $T_{\varepsilon}$ satisfying $T_{\varepsilon} \leq \frac{|\varepsilon(0^+)|}{C_3}$.

## REFERENCES


[1] B. Subudhi and R. Pradhan, "A comparative study on maximum power point tracking techniques for photovoltaic power systems," *IEEE Trans. Sustain. Energy*, vol. 4, no. 1, pp. 89–98, Jan. 2013.

[2] M. A. G. de Brito, L. Galotto, L. P. Sampaio, G. de Azevedo e Melo, and C. A. Canesin, "Evaluation of the main MPPT techniques for photovoltaic applications," *IEEE Trans. Ind. Electron.*, vol. 60, no. 3, pp. 1156–1167, Mar. 2013.

[3] D. Sera, L. Mathe, T. Kerekes, S. V. Spataru, and R. Teodorescu, "On the perturb-and-observe and incremental conductance MPPT methods for PV systems," *IEEE J. Photovolt.*, vol. 3, no. 3, pp. 1070–1078, Jul. 2013.

[4] S. B. Kjaer, "Evaluation of the "Hill Climbing" and the "Incremental Conductance" maximum power point trackers for photovoltaic power systems," *IEEE Trans. Energy Convers.*, vol. 27, no. 4, pp. 922–929, Dec. 2012.

[5] C. B. Salah and M. Ouali, "Comparison of Fuzzy logic and neural network in maximum power point tracker for PV systems," *Elect. Power Syst. Res.*, vol. 81, pp. 43–50, 2011.

[6] T. Esram and P. L. Chapman, "Comparison of photovoltaic array maximum power point tracking techniques," *IEEE Trans. Energy Convers.*, vol. 22, no. 2, pp. 439–449, Jun. 2007.

[7] S. Jain and V. Agarwal, "Comparison of the performance of maximum power point tracking schemes applied to single-stage grid-connected photovoltaic systems," *IET Elect. Power Appl.*, vol. 1, no. 5, pp. 753–762, Sep. 2007.

[8] V. Salas, E. Olias, A. Barrado, and A. Lázaro, "Review of the maximum power point tracking MPPTs for stand-alone photovoltaic systems," *Solar Energy Mater. Solar Cells*, vol. 90, pp. 1555–1578, 2006.

[9] D. P. Hohm and M. E. Ropp, "Comparative study of maximum power point tracking algorithms," *Progr. Photovolt., Res. Appl.*, vol. 11, no. 1, pp. 47–62, Nov. 2002.

[10] L. V. Hartmann, M. A. Vitorino, M. B. R. Correa, and A. M. N. Lima, "Combining model-based and heuristic techniques for fast tracking the maximum-power point of photovoltaic systems," *IEEE Trans. Power Electron.*, vol. 28, no. 6, pp. 2875–2885, Jun. 2013.

[11] K.-J. Lee and R.-Y. Kim, "An adaptive maximum power point tracking scheme based on a variable scaling factor for photovoltaic systems," *IEEE Trans. Energy Convers.*, vol. 27, no. 4, pp. 1002–1008, Dec. 2012.

[12] A. Chikh and A., "An optimal maximum power point tracking algorithm for PV systems with climatic parameters estimation," *IEEE Trans. Sustain. Energy*, vol. 6, no. 2, pp. 644–652, Apr. 2015.

[13] Y. Jiang, J. A. A. Qahouq, and T. A. Haskew, "Adaptive step size with adaptive-perturbation-frequency digital MPPT controller for a single-sensor photovoltaic solar system," *IEEE Trans. Power Electron.*, vol. 28, no. 7, pp. 3195–3205, Jul. 2013.

[14] K. K. Tse, B. M. T. Ho, H. S.-H. Chung, and S. Y. Ron Hui, "A comparative study of maximum-power-point-trackers for photovoltaic panels using switching-frequency modulation scheme," *IEEE Trans. Ind. Electron.*, vol. 51, no. 2, pp. 410–418, Apr. 2004.

[15] K. K. Tse, M. T. Ho, H. S.-H. Chung, and S. Y. R. Hui, "A novel maximum power point tracker for PV panels using switching frequency modulation," *IEEE Trans. Power Electron.*, vol. 17, no. 6, pp. 980–989, Nov. 2002.

[16] H.-S. Bae, J.-H. Park, B.-H. Cho, and G.-J. Yu, "New MPPT control strategy for two-stage grid-connected photovoltaic power conditioning system," *J. Power Electron.*, vol. 7, no. 2, pp. 174–180, 2007.

[17] H. S.-H. Chung, K. K. Tse, S. Y. R. Hui, C. M. Mok, and M. T. Ho, "A novel maximum power point tracking technique for solar panels using a SEPIC or Cuk converter," *IEEE Trans. Power Electron.*, vol. 18, no. 3, pp. 717–724, May 2003.

[18] M. Veerachary, T. Senjyu, and K. Uezato, "Maximum power point tracking of coupled inductor interleaved boost converter supplied PV system," *IEE Proc. Elect. Power Appl.*, vol. 150, no. 1, pp. 71–80, Jan. 2003.

[19] K. L. Lian, J. H. Jhang, and I. S. Tian, "A maximum power point tracking method based on perturb-and-observe combined with particle swarm optimization," *IEEE J. Photovolt.*, vol. 4, no. 2, pp. 626–633, Mar. 2014.

[20] D. C. Jones and R. W. Erickson, "Probabilistic analysis of a generalized perturb and observe MPPT featuring robust operation in the presence of power curve traps," *IEEE Trans. Power Electron.*, vol. 28, no. 6, pp. 2912–2926, Jun. 2013.

[21] A. El Khateb, N. A. Rahim, J. Selvaraj, and M. N. Uddin, "Maximum power point tracking of single-ended primary-inductor converter employing a novel optimization technique for proportional-integral-derivative controller," *IET Power Electron.*, vol. 6, no. 6, pp. 1111–1121, Jul. 2013.

[22] G. Carannante, C. Fraddanno, M. Pagano, and L. Piegari, "Experimental performance of MPPT for photovoltaic sources subject to inhomogeneous insolation," *IEEE Trans. Ind. Electron.*, vol. 56, no. 11, pp. 4374–4380, Nov. 2009.

[23] N. Fermia, G. Petrone, G. Spagnuolo, and M. Vitelli, "A technique for Improving P&O MPPT performances of double-stage grid-connected photovoltaic systems," *IEEE Trans. Ind. Electron.*, vol. 56, no. 11, pp. 4473–4482, Nov. 2009.

[24] D. Sera, R. Teodorescu, J. Hantschel, and M. Knoll, "Optimized maximum power point tracker for fast-changing environmental conditions," *IEEE Trans. Ind. Electron.*, vol. 55, no. 7, pp. 2629–2637, Jul. 2008.

[25] R. Faraji, A. Rouholamini, H. R. Naji, R. Fadaeinedjad, and M. R. Chavoshian, "FPGA-based real time incremental conductance maximum power point tracking controller for photovoltaic systems," *IET Power Electron.*, vol. 7, no. 5, pp. 1294–1304, May 2014.

[26] M. A. Elgendy, B. Zahawi, and D. J. Atkinson, "Assessment of the incremental conductance maximum power point tracking MPPT," *IEEE Trans. Sustain. Energy*, vol. 4, no. 1, pp. 108–117, Jan. 2013.

[27] H. Guan-Chyun, H. Hung-I Hsieh, T. Cheng-Yuan, and W. Chi-Hao, "Photovoltaic power-increment-aided incremental-conductance MPPT with two-phased tracking," *IEEE Trans. Power Electron.*, vol. 28, no. 6, pp. 2895–2911, Jun. 2013.

[28] G. J. Kish, J. J. Lee, and P. W. Lehn, "Modelling and control of photovoltaic panels utilizing the incremental conductance method for maximum power point tracking," *IET Renewable Power Gener.*, vol. 6, no. 4, pp. 259–266, Jul. 2012.

[29] A. Safari and S. Mekhilef, "Simulation and hardware implementation of incremental conductance MPPT with direct control method using Cuk converter," *IEEE Trans. Ind. Electron.*, vol. 58, no. 4, pp. 1154–1161, Apr. 2011.

[30] Q. Mei, M. Shan, L. Liu, and J. M. Guerrero, "A novel improved variable step-size incremental-resistance MPPT method for PV systems," *IEEE Trans. Ind. Electron.*, vol. 58, no. 6, pp. 2427–2434, Jun. 2011.

[31] A. El Khateb, N. Abd Rahim, J. Selvaraj, and M. N. Uddin, "Fuzzy-Logic-Controller-Based SEPIC converter for maximum power point tracking," *IEEE Trans. Ind. Appl.*, vol. 50, no. 4, pp. 2349–2358, Jul. 2014.

[32] M. A. A. Mohd Zainuri, M. A. Mohd Radzi, A. C. Soh, and N. A. Rahim, "Development of adaptive perturb and observe-fuzzy control maximum power point tracking for photovoltaic boost dc-dc converter," *IET Renewable Power Gener.*, vol. 8, no. 2, pp. 183–194, Mar. 2014.

[33] F. Chekired, C. Larbes, D. Rekioua, and F. Haddad, "Implementation of a MPPT Fuzzy controller for photovoltaic synthesis on FPGA circuit," *Energy Procedia*, vol. 6, pp. 541–549, 2011.

[34] B. N. Alajmi, K. H. Ahmed, S. J. Finney, and B. W. Williams, "Fuzzy-Logic-Control approach of a modified hill-climbing method for maximum power point in microgrid standalone photovoltaic system," *IEEE Trans. Power Electron.*, vol. 26, no. 4, pp. 1022–1030, Apr. 2011.

[35] P. E. Kakosimos, A. G. Kladas, and S. N. Manias, "Fast photovoltaic-system voltage- or current-oriented MPPT employing a predictive digital current-controlled converter," *IEEE Trans. Ind. Electron.*, vol. 60, no. 12, pp. 5673–5685, Dec. 2013.

[36] K. Sundareswaran, S. Peddapati, and S. Palani, "Application of random search method for maximum power point tracking in partially shaded photovoltaic systems," *IET Renewable Power Gener.*, vol. 8, no. 6, pp. 670–678, Aug. 2014.

[37] A. M. Bazzi and P. T. Krein, "Ripple correlation control: an extremum seeking control perspective for real-time optimization," *IEEE Trans. Power Electron.*, vol. 29, no. 2, pp. 988–995, Feb. 2014.

[38] J. W. Kimball and P. T. Krein, "Discrete-time ripple correlation control for maximum power point tracking," *IEEE Trans. Power Electron.*, vol. 23, no. 5, pp. 2353–2362, Sep. 2008.

[39] T. Esram, J. W. Kimball, P. T. Krein, P. L. Chapman, and P. Midya, "Dynamic maximum power point tracking of photovoltaic arrays using ripple correlation control," *IEEE Trans. Power Electron.*, vol. 21, no. 5, pp. 1282–1291, Sep. 2006.

[40] H. Zazo, R. Leyva, and E. del Castillo, "MPPT based on newton-like extremum seeking control," in *Proc. IEEE Int. Symp. Ind. Electron.*, 2012, pp. 1040–1045.

[41] X. Li, Y. Li, and J. E. Seem, "Maximum power point tracking for photovoltaic system using adaptive extremum seeking control," *IEEE Trans. Control Syst. Technol.*, vol. 21, no. 6, pp. 2315–2322, Nov. 2013.

[42] A. M. Bazzi and P. T. Krein, "Concerning maximum power point tracking for photovoltaic optimization using ripple-based extremum seeking control," *IEEE Trans. Power Electron.*, vol. 26, no. 6, pp. 1611–1612, Jun. 2011.

[43] S. L. Brunton, C. W. Rowley, S. R. Kulkarni, and C. Clarkson, "Maximum power point tracking for photovoltaic optimization using ripple-based extremum seeking control," *IEEE Trans. Power Electron.*, vol. 25, no. 10, pp. 2531–2540, Oct. 2010.

[44] R. Leyva, C. Alonso, I. Queinnec, A. Cid-Pastor, D. Lagrange, and L. Martinez-Salamero, "MPPT of photovoltaic systems using Extremum - seeking control," *IEEE Trans. Aerosp. Electron. Syst.*, vol. 42, no. 1, pp. 249–258, Jan. 2006.

[45] C. Cabal, L. Martinez-Salamero, L. Seguier, C. Alonso, and F. Guinjoan, "Maximum power point tracking based on sliding-mode control for output-series connected converters in photovoltaic systems," *IET Power Electron.*, vol. 7, no. 4, pp. 914–923, 2014.

[46] H.-T. Yau, C.-J. Lin, and C.-H. Wu, "Sliding mode extremum seeking control scheme based on PSO for maximum power point tracking in photovoltaic systems," *Int. J. Photoenergy*, vol. 2013, pp. 1–10, 2013.

[47] E. Bianconi *et al.*, "A fast current-based MPPT technique employing sliding mode control," *IEEE Trans. Ind. Electron.*, vol. 60, no. 3, pp. 1168–1178, Mar. 2013.

[48] Y. Levron and D. Shmilovitz, "Maximum power point tracking employing sliding mode control," *IEEE Trans. Circuits Syst. I, Reg. Papers*, vol. 60, no. 3, pp. 724–732, Mar. 2013.

[49] C.-C. Chu and C.-L. Chen, "Robust maximum power point tracking method for photovoltaic cells: A sliding mode control approach," *Solar Energy*, vol. 83, pp. 1370–1378, 2009.

[50] J. M. Blanes, F. Javier Toledo, S. Moreno, and A. Garrigós, "In-Site real-time photovoltaic I-V curves and maximum power point estimator," *IEEE Trans. Power Electron.*, vol. 28, no. 3, pp. 1234–1240, Mar. 2013.

[51] G. Spagnuolo, G. Petrone, B. Lehman, C. A. Ramos Paja, Y. Zhao, and M. L. Orozco Gutierrez, "Control of photovoltaic arrays: Dynamical reconfiguration for fighting mismatched conditions and meeting load requests," *IEEE Ind. Electron. Mag.*, vol. 9, no. 1, pp. 62–76, Mar. 2015.

[52] K. Chen, S. Tian, Y. Cheng, and L. Bai, "An improved MPPT controller for photovoltaic system under partial shading condition," *IEEE Trans. Sustain. Energy*, vol. 5, no. 3, pp. 978–985, Jul. 2014.

[53] S. Moballegh and J. Jiang, "Modeling, prediction, and experimental validations of power peaks of PV arrays under partial shading conditions," *IEEE Trans. Sustain. Energy*, vol. 5, no. 1, pp. 293–300, Jan. 2014.

[54] K.-S. Tey and S. Mekhilef, "Modified incremental conductance algorithm for photovoltaic system under partial shading conditions and load variation," *IEEE Trans. Ind. Electron.*, vol. 61, no. 10, pp. 5384–5392, Oct. 2014.

[55] S. Maity and P. K. Sahu, "Modeling and analysis of a fast and robust module-integrated analog photovoltaic MPP tracker," *IEEE Trans. Power Electron.*, vol. 31, no. 1, pp. 280–291, Jan. 2016.

[56] T.-K. Soon and S. Mekhilef, "A fast-converging MPPT technique for photovoltaic system under fast-varying solar irradiation and load resistance," *IEEE Trans. Ind. Informat.*, vol. 11, no. 1, pp. 176–186, Feb. 2015.

[57] J. S. C. M. Raj and A. E. Jeyakumar, "A novel maximum power point tracking technique for photovoltaic module based on power plane analysis of - characteristics," *IEEE Trans. Ind. Electron.*, vol. 61, no. 9, pp. 4734–4745, Sep. 2014.

[58] S. K. Kollimalla and M. K. Mishra, "Variable perturbation size adaptive P&O MPPT for sudden changes in irradiance," *IEEE Trans. Sustain. Energy*, vol. 5, no. 3, pp. 718–728, Jul. 2014.

[59] S. K. Kollimalla and M. K. Mishra, "A novel adaptive P&O MPPT algorithm considering sudden changes in the irradiance," *IEEE Trans. Energy Convers.*, vol. 29, no. 3, pp. 602–610, Sep. 2014.

[60] K. Soon Teya and S. Mekhilef, "Modified incremental conductance MPPT for photovoltaic system under partial shading conditions and load variation," *IEEE Trans. Ind. Electron.*, vol. 61, no. 10, pp. 5384–5392, Oct. 2014.

[61] S. Maity and P. K. Sahu, "Modeling and analysis of a fast and robust module-integrated analog photovoltaic MPP tracker," *IEEE Trans. Power Electron.*, vol. 31, no. 1, pp. 280–291, Jan. 2016.

[62] R. Haroun, A. Cid-Pastor, A. El Aroudi, and L. Martinez-Salamero, "Synthesis of canonical elements for power processing in DC distribution systems using cascaded converters and sliding-mode control," *IEEE Trans. Power Electron.*, vol. 29, no. 3, pp. 1366–1381, Mar. 2014.

[63] A. Cid-Pastor, L. Martinez-Salamero, A. El Aroudi, R. Giral, J. Calvente, and R. Leyva, "Synthesis of loss-free resistors based on sliding-mode control and its applications in power processing," *Control Eng. Practice*, vol. 21, no. 5, pp. 689–699, May 2013.

[64] R. Haroun, A. El Aroudi, A. Cid-Pastor, G. Garcia, C. Olalla, and L. Martinez-Salamero, "Impedance matching in photovoltaic systems using cascaded boost converters and sliding-mode control," *IEEE Trans. Power Electron.*, vol. 30, no. 6, pp. 3185–3199, Jun. 2015.

[65] S. Singer and R. W. Erickson, "Canonical modeling of power processing circuits based on the POPI concept," *IEEE Trans. Power Electron.*, vol. 7, no. 1, pp. 37–43, Jan. 1992.
[66] J. S. C. M. Raj and A. E. Jeyakumar, "A novel maximum power point tracking technique for photovoltaic module based on power plane analysis of – characteristics," *IEEE Trans. Ind. Electron.*, vol. 61, no. 9, pp. 4734–4745, Sep. 2014.
[67] A. H. Alqahtani and V. I. Utkin, "Self-optimization of photovoltaic system power generation based on sliding mode control," in *Proc. 38th Annu. Conf. IEEE Ind. Electron. Soc.*, 2012, pp. 3468–3474.
[68] S. P. Bhat and D. S. Bernstein, "Finite-time stability of continuous autonomous systems," *SIAM J. Control Optim.*, vol. 38, no. 3, pp. 751–766, 2000.
[69] F.-S. Pai, R.-M. Chao, S. H. Ko, and T.-S. Lee, "Performance evaluation of parabolic prediction to maximum power point tracking for PV array," *IEEE Trans. Sustain. Energy*, vol. 2, no. 1, pp. 60–68, Jan. 2011.
[70] O. Lopez-Santos, L. Martinez-Salamero, G. Garcia, and H. Valderrama-Blavi, "Sliding-mode control of a transformer-less dual-stage grid-connected photovoltaic micro-inverter," in *Proc. 10th Int. Multi-Conf. Syst., Signals, Devices*, 2013, pp. 1–6.
[71] O. Lopez-Santos, L. Martinez-Salamero, G. Garcia, H. Valderrama-Blavi, and D. Mercury, "Efficiency analysis of a sliding-mode controlled quadratic boost converter," *IET Power Electron.*, vol. 6, no. 2, pp. 364–373, Jun. 2013.
[72] D. P. Ohm and M. E. Ropp, "Comparative study of maximum power point tracking algorithms," *Progr. Photovolt., Res. Appl.*, vol. 11, no. 1, pp. 47–62, Jan. 2003.
[73] S. M. Reza Tousi, M. H. Moradi, N. S. Basir, and M. Nemati, "A function-based maximum power point tracking method for photovoltaic systems," *IEEE Trans. Power Electron.*, vol. 31, no. 3, pp. 2120–2128, Mar. 2016.
[74] N. Femia, G. Petrone, G. Spagnuolo, and M. Vitelli, *Power Electronics and Control Techniques for Maximum Energy Harvesting in Photovoltaic Systems*. Boca Raton, FL, USA: CRC Press, 2012.

**Oswaldo Lopez-Santos** (S'00–M'15–SM'17) received the B.S. degree in electronics engineering from the Universidad Distrital Francisco José de Caldas in Bogotá, Colombia, in 2002, the M.S. degree in industrial automation from the Universidad Nacional de Colombia, Bogotá, Colombia, in 2011, and the Ph.D. degree in automation from Institut National des Sciencies Apliquées (INSA), Toulouse, France, enrolled with the Laboratoire d'Analyse et d'Architecture des Systemès (LAAS-CNRS).

From 2004 to 2008, he worked in Colombia as Power Electronics Designer in the production of UPS, inverters, and power rectifiers. He is currently an Associate Professor with the Programa de Ingeniería Electrónica, Universidad de Ibagué, Colombia. His current research focuses on control of power electronics converters for renewable energy applications and microgrids.

**Germain Garcia** received the Diploma degree in engineering from the Institut National des Sciencies Apliquées (INSA), Toulouse, France, in 1984. He received the Ph.D. degree in automatic control from the INSAT in 1988 and the Habilitation à Diriger des Recherches (HDR) in 1997 from the same university.

He is currently at the Laboratoire d'Architecture des Systèmes of the Centre National pour la Recherche Scientifique (LAAS-CNRS), Toulouse, France, as a Full Professor of INSAT. His research interests include robust control theory, linear matrix inequalities (LMI), constrained control, and singularity perturbed models.

**Luis Martinez-Salamero** (M'79–SM'86) received the Ingeniero de Telecomunicación degree in 1978 and the Ph.D. degree in 1984, both from the Universidad Politécnica de Cataluña, Barcelona, Spain.

From 1978 to 1992, he taught circuit theory, analog electronics, and power processing at the Escuela Técnica Superior de Ingenieros de Telecomunicación de Barcelona, Barcelona, Spain. From 1992 to 1993, he was a Visiting Professor at the Center for Solid State Power Conditioning and Control, Department of Electrical Engineering, Duke University, Durham, NC, USA. From 2003 to 2004 and 2010 to 2011, he was a Visiting Scholar at the Division of Power Devices and Power Integration, Laboratory of Architecture and Systems Analysis (LAAS), National Agency for Scientific Research (CNRS), Toulouse, France. Since 1995, he has been a Full Professor with the Department of Electrical Electronic and Automatic Control Engineering, School of Electrical and Computer Engineering, Rovira i Virgili University, Tarragona, Spain, where he managed the Research Group in Automatic Control and Industrial Electronics (GAEI) in the period 1998–2018. His research interests include structure and control of power conditioning systems, namely, electrical architecture of satellites and electric vehicles, as well as nonlinear control of converters and drives, and power conditioning for renewable energy.

**Roberto Giral** (S'94–M'02–SM'10) received the B.S. degree in Ingeniería Técnica de Telecomunicación, the M.S. and Ph.D (Hons.) degrees in Ingeniería de Telecomunicación from the Universitat Politècnica de Catalunya, Barcelona, Spain, in 1991, 1994, and 1999, respectively.

He is currently an Associate Professor in the Departament d'Enginyeria Electrònica, Elèctrica i Automàtica, Escola Tècnica Superior d' Enginyeria, Universitat Rovira i Virgili, Tarragona, Spain, where he is working in the field of power electronics.

**Enric Vidal-Idiarte** (S'97–M'04) received the Licenciado en Informatica and Ph.D. degrees from the UPC, Barcelona, Spain, in 1993 and 2001, respectively.

He is currently an Associate Professor with the Departament d'Enginyeria Electronica, Electrica i Automatica,

Universitat Rovira i Virgili, Tarragona, Spain, where he is working in the field of digital and robust control of power converters. He is a Member of the Grup d´Automàtica i Electrònica Industrial Research Group on Industrial Electronics and Automatic Control, whose main research fields are power conditioning for vehicles, satellites, and renewable energy.

**Maria Camila Merchan-Riveros** (S'17) received the Electronics Engineer's degree from the Universidad de Ibagué, Ibagué, Colombia, in 2016. She is currently working toward the Master's degree in control engineering, being a member in the Research Group D+Tec, Universidad de Ibagué.

She finished her undergraduate studies as a Research Assistant in the Research Group D+Tec, of the Universidad de Ibagué, involved in the field of digital control of power converters applied in photovoltaic systems. Her research interests include control of linear and nonlinear systems, instrumentation and development of digital control, supervision systems, and computer applications for power systems.

**Yamel Moreno-Guzmán** received the Electronics Engineer's degree from the Universidad de Ibagué, Ibagué, Colombia, in 2013. He finished his undergraduate studies as a research assistant in the Research Group D+Tec, of the Universidad de Ibagué.